Title
Numerical Investigation of Dynamic Stall using Delayed Detached Eddy Simulations

Author
Batther, Jagdeep Singh

Publication Date
2021

Peer reviewed|Thesis/dissertation

Numerical Investigation of Dynamic Stall using Delayed Detached Eddy Simulations

By

JAGDEEP BATTHER

THESIS

Submitted in partial satisfaction of the requirements for the degree of

MASTER OF SCIENCE

in

Mechanical & Aerospace Engineering

in the

OFFICE OF GRADUATE STUDIES

of the

UNIVERSITY OF CALIFORNIA

DAVIS

Approved:

Seongkyu Lee, Chair

Mohamed Hafez

C.P. van Dam

Committee in Charge

2021

TABLE OF CONTENTS

LIST OF FIGURES

LIST OF TABLES

ACKNOWLEDGMENTS

The completion of this investigation could not have been possible without the guidance of Dr. Seongkyu Lee, and support from my family and friends.

NOMENCLATURE

DSV	=	Dynamic Stall Vortex
LSB	=	Laminar Separation Bubble
LEV	=	Leading-Edge Vortex
TEV	=	Trailing-Edge Vortex
TKE	=	Turbulent Kinetic Energy
LES	=	Large Eddy Simulation
DNS	=	Direct Numerical Simulation
$DDES$	=	Delayed Detached Eddy Simulation
CGT	=	Chimera Grid Tools
AFT	=	Amplification Factor Transport
α	=	Dynamic Stall Vortex
C_p, C_f	=	Pressure and Skin Friction Coefficient
Re	=	Reynolds Number
M	=	Mach Number
u, v, w	=	Velocity Components
ω_x, ω_y, ω_z	=	Vorticity Components
x,y,z	=	Cartesian Coordinates
C_L, C_D, C_M	=	Lift. Drag, and Pitching Moment Coefficients
SST	=	Shear Stress Transport
SA	=	Spalart Allmarras
t	=	Time (s)
t^*	=	Non-dimensional Time
Δt^*	=	Non-dimensional Time Step
Ψ	=	Pitch Rate (rad/s)
$\Psi_\circ^+$	=	Non-dimensional Pitch Rate

ABSTRACT

This thesis examines the feasibility of Delayed Detached Eddy Simulations (DDES) in terms of predicting aerodynamic loads and capturing complex flow physics relating to the dynamic stall process at a transitional Reynolds number of $200,000$ and Mach number of 0.10, using NASA's OVERFLOW 2.3 code. This investigation tests the performance and capabilities of state-of-the-art transition models in terms of their ability to capture the underlying viscous mechanisms from which dynamic stall is onset. This work focuses on the events leading up to stall, rather than the analysis of the stalled flow itself, hence the focus will be on the upstroke region. This is due to the modern-day modeling tools being more so calibrated for pre-stall. Furthermore, an accurate prediction of the pre-stall regime could have a significant impact in employing flow control technologies in the future. All grids generated are based on current best practices of Chimera Grid Tools (CGT). While current Large Eddy Simulations (LES) standards recommend a low y^+ value in the boundary layer, a conservative value of 0.4 is used. Deeper investigations into the flow physics are performed on the 2nd finest grid out of 3 configurations. While by nature it would be expected that the finest mesh would yield the most accurate results, another motivation for this study is to test capabilities performed on a scale parallel with current industry standards, using coarser meshes, and lower fidelity models, resulting in quicker turnaround times. It is found that the overall flow physics is captured in detail even with a mesh composed of roughly 16 million grid points. A leading-edge separation region and formation of a dynamic stall vortex is examined in detail, and results suggest that the role of a laminar separation bubble is significant in the dynamic stall process, which has otherwise been a controversial point in the past regarding this flow phenomenon. Furthermore, it is found that DDES matches up accurately with respect to benchmark LES results for the same case, but with coarser spatial and temporal resolutions. James Coder's SA Amplification Factor Transport (AFT) transition model yielded the most accurate results when compared with LES results and shows promising results for future

use in more high-fidelity case studies. Langtry and Menter's SST correlation-based transition ($\gamma - \tilde{Re}_{\theta t}$) model and its SA counterpart developed by Medida and Baeder are also investigated in detail.

Chapter 1

Introduction

1.1 Motivation

Dynamic stall is a complex flow phenomenon that occurs in the realm of rapid maneuvering fixed and rotary-wing aircraft, turbomachinery, and wind turbines. It is characterized by a delay in the onset of boundary layer separation on a blade subject to transient alterations in angle of attack beyond the static stall angle, which increases aerodynamic loads considerably larger than those associated with static stall. When stall itself is onset, there is a massive flow separation on the upper surface that results in a gradual or abrupt loss of lift, an increase in drag, and a large nose down pitching moment, severely impeding the performance of the aircraft. Focusing on the realm of rotorcraft, it is a direct result due to the cyclic pitch applied to the rotor blades for maintaining a balanced thrust force across the entire rotor disk. The unsteady loading and vibrations encountered during dynamic stall severely hinder the performance, as it restricts forward flight limits and compromises the structural integrity of the rotor blades. Due to the chaotic nature of this flow phenomenon, it remains a very difficult task to accurately capture and predict through experimental and computational

methods [1]. In rotorcraft, DDES has been widely used to predict dynamic stall, however, the focus was more geared towards the aerodynamic performance rather than the in-depth flow physics. The predictive capabilities of DDES in terms of capturing the complex flow features, such as the onset of the dynamic stall vortex (DSV) has not yet been reported in detail. Smith [2] provided a comprehensive discussion on the current state of knowledge regarding this flow phenomenon. Despite the tremendous progress that has been made in this field of study, further knowledge is still required. Some of the conclusions/recommendations from [2] are listed:

- Two-dimensional dynamic stall must be solved in three-dimensional space to capture the separation region. Purely two-dimensional computations exhibit stronger, non-physical responses that impact the ability to capture the onset of dynamic stall.
- Integration of computational studies with coordinated experimental studies will provide results that are valuable for code validation. Combined use of validated computational results and high-quality experimental results are likely to yield the greatest advancement in understanding.
- A better understanding of the timing and impact of dynamic stall flow features under different conditions and combinations of conditions, such as unsteady inflow, aeroelasticity, wake interactions, boundary layer transition, and airfoil shape, is needed.

Currently, LES [1] has proven to be the most effective in capturing important flow features during the dynamic stall process, however the required computational resources make it impractical for industry use. This thesis aims to focus on the point of understanding the viscous mechanisms from which dynamic stall is onset using DDES, which provides much faster solutions than LES. This work will investigate the feasibility of using DDES for capturing the distinct flow features that are associated with the dynamic stall process for a low Reynolds number case ($M = 0.10$, $Re = 200{,}000$). Having the ability to understand the

process from which this flow phenomenon occurs at a reasonable computational cost has massive implications for the practical study of flow control technologies which could in turn increase forward flight limits of rotorcraft in the future. Moreover, this thesis will test the capabilities of state-of-the-art turbulence and transition models in terms of capturing the complex flow physics associated with dynamic stall.

1.2 Rotorcraft Aerodynamics

What sets helicopters apart is the capability to perform vertical takeoff and landing (VTOL), which allows for a wide array of possibilities in terms of destinations they can travel [3]. Their operation is much more complex than conventional fixed wing aircraft. These aircraft generate lift through the rotation of the blades which generates complex flow features due to the asymmetric aerodynamic loading distribution in forward flight. A general perspective of the rotorcraft can be seen in Fig. 1. There exists an advancing side and retreating side of the rotor. It can be seen from the schematic that there is a relative velocity difference on both ends of the rotor disk. This requires the retreating side to operate at a higher angle of attack to offset the difference in flow velocity, and thereby maintain a uniform thrust across the rotor.

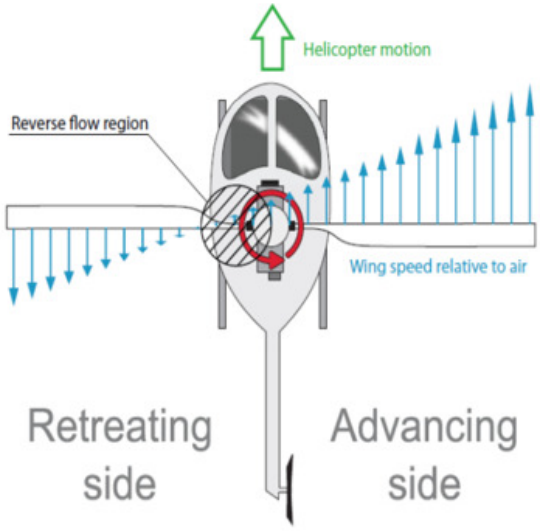

Figure 1: Overview of rotor disk [4].

1.3 Dynamic Stall

1.3.1 Characteristics

As previously discussed, when there exist transient changes in angle of attack due to the cyclic pitch in rotorcraft or rapid maneuvering fixed wing flight, the maximum lift exceeds well beyond the static stall angle. McCroskey [5] classified dynamic stall into two main categories based on the angle of attack.

- Light Stall: Encountered when the angle of attack is only slightly greater than the static stall angle of attack. In this realm the separated flow region is relatively small.
- Deep Stall: Encountered when the angle of attack is much greater than the static stall angle. In this regime, there is a formation of a leading-edge vortex (LEV), which causes large overshoots in the aerodynamics loads until the point where the vortex sheds off the blade surface, and the blade is in a fully stalled state.

Not only are the physical elements of the aircraft compromised when dynamic stall is onset, but this phenomenon also has a large effect on the aircraft control systems. The large fluctuations in the aerodynamic loads can cause excessive inputs into the control system, compromising the vehicle dynamics to a point where the vehicle can go into a dangerous spin state. There are two distinct physical processes that trigger the onset of dynamic stall:

- Leading Edge Stall: In leading-edge stall, McCroskey et al. [6] identifies two different processes from which the stall is initiated. The first is through a formation of a laminar separation bubble (LSB) at the leading edge that contracts with increasing angle of incidence, to a point at which it is no longer able to facilitate reattachment due to the large adverse pressure gradient. This results in a sudden separation of the boundary

layer due to the bursting of the LSB, otherwise known as "pressure-gradient bubble bursting" stall. The second form occurs due to the rapid propagation of the separated flow upstream, with the presence of a LSB at the leading edge. Here, the separated flow meets the LSB causing abrupt breakdown of suction at the leading edge. This is known as "turbulent leading-edge stall". Both types of leading-edge stall are associated with abrupt lift and moment stalls as well as a hysteresis between pitching directions.

- Trailing Edge Stall: Trailing-edge stall, by contrast, occurs in a situation of no LSB or a stable LSB and describes the relatively slow upstream propagation of turbulent boundary-layer separation from the airfoil trailing edge up to the leading edge, resulting in gradual lift and moment stall with little hysteresis [6].

The stall development process is quite different when compared static and dynamically pitching airfoils. The detailed flow features that have proven to be common for most airfoils pitched dynamically will be discussed. The different stages of the dynamic stall process associated with classical trailing-edge stall can be seen in Fig. 2. This was from an experiment performed by McCroskey et al. [6] on a NACA 0012 airfoil section. Point (a) signifies the blade passing the static stall angle. At this point, there are no detectable changes in the flow over the blade as the boundary layer remains thin with no signs of flow reversal. Point (b) is when flow reversal is identified towards the trailing edge, and the boundary layer begins to thicken. At point (d) the flow reversal propagates upstream from the trailing edge, causing a region of disturbed boundary layer flow. At this point there is still not significant alterations in the predicted aerodynamic loads. Point (e) signifies flow separation at the leading edge, where suction is lost, and the process of the dynamic stall vortex formation begins. As the vortex forms and propagates downstream the pitching moment starts to diverge from its static values. At point (f) the lift-curve slope increases, showing a behavior different from its static counterpart, and the lift keeps increasing with increasing angle of incidence, exceeding the value of the static lift curve slope of $2\pi/radian$. Point (g) indicates the onset of moment

stall, where a large nose down pitching moment is induced. Lastly, point (h) signifies the onset of lift stall, where the maximum lift coefficient is reached, followed by a sharp decrease. At this point the DSV is at approximately mid-chord [6].

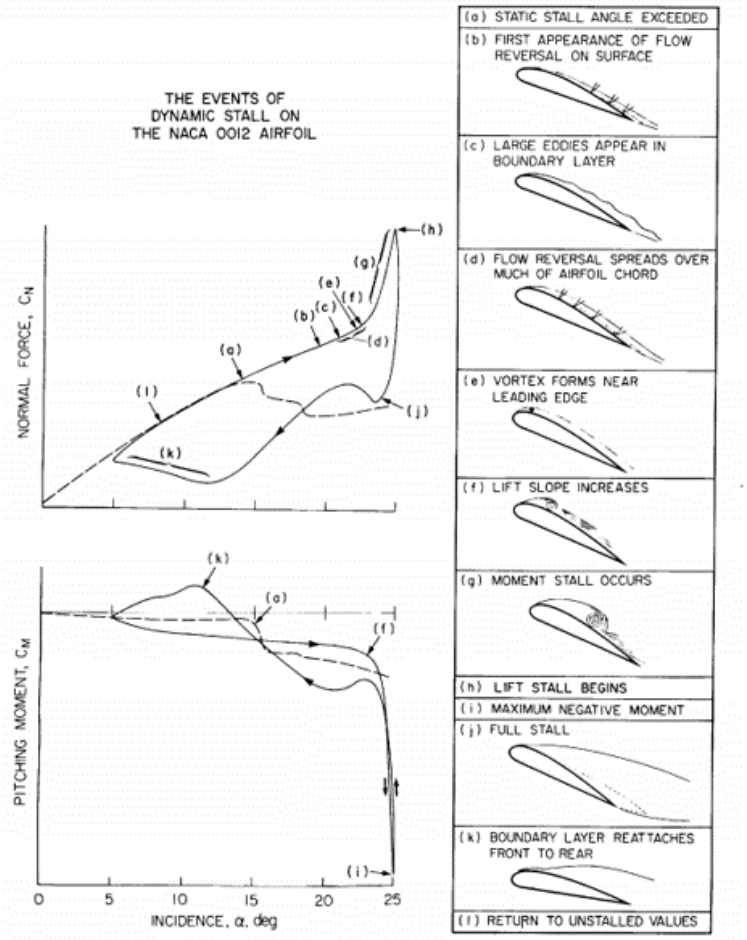

Figure 2: Different stages of dynamic stall [6].

1.3.2 Literature Review

Dynamic stall has been an active research topic for more than half a century. This research came about when classical unsteady aerodynamic theory had been developed by researchers such as Wagner (1925), Glauert (1929), Theodorsen (1935), and many others. During this time, studies were launched where researchers developed analytical solutions to incompress-

ible flow over thin airfoils undergoing time-dependent motion. Unsteady aerodynamics had to first be realized by researchers since conventional aerodynamics at that time could not sufficiently explain why helicopters were experiencing higher magnitudes of lift than expected with a conventional, or steady aerodynamics approach. Kramer (1932) was one of the first to experimentally document the augmented lift associated with dynamic stall [7] but couldn't pinpoint the exact reason for which it occurred. Ham and Garelick [8] observed that extra lift could be generated through rapid pitching of airfoils, and that this overshoot was associated with a vortex formed on the airfoil during the unsteady motion. The analysis of dynamic stall events on an oscillating airfoil by Carr [7] revealed that the prominent features within a full cycle of oscillation are consecutively the emergence and spreading of flow reversal on the airfoil's suction side, the formation and convection of a large-scale leading-edge vortex, massive flow separation, and flow reattachment. During this time (1977), a pivotal study in this field was conducted by McCroskey et al. [6] where the analysis of the onset of dynamic stall for a variety of different Reynolds numbers, and airfoil configurations was conducted. This was following a time period where a handful of researchers were observing both leading edge and trailing edge stall for a variety of flow conditions and geometries. One of the most important takeaways from this study was the fact that they were experimentally able to identify two forms of leading-edge stall: one of which consisted of the pressure-gradient induced bursting of a LSB formed at the leading edge, and the second being the rapid propagation of the trailing edge separation upstream, to the point where it caused the collapse of a LSB that developed on the leading-edge. This rapid propagation of the reversed flow upstream was classified under leading-edge stall since trailing-edge stall is a more gradual propagation of the separated flow upstream. This was after many researchers were associating leading-edge stall solely due to pressure-gradient bursting of the LSB, classifying this observation as a new type of leading-edge stall. Moreover, they identified the large influence of Reynolds number on the overall flow physics and different types of stall noted from researchers prior to this study. In decades following, many researchers validated the early

findings of McCroskey et al. [6], Carr [7], and Ham and Garelick [8], such as Shih et al. [9], who classified the unsteady flow development over an airfoil pitching up at constant rate into four successive stages: a vortex formation stage, a vortex convection stage, stall onset, and a stalled stage. These findings show that the flow over either a constantly pitching or oscillating airfoil is qualitatively described by the same characteristic features, being the initiation, growth and shedding of a leading-edge vortex and the associated lift overshoot. In the time period following the publication of many groundbreaking discoveries related to dynamic stall, many experimental techniques were applied, including flow visualizations, force measurements, surface pressure, hot-film measurements, planar whole field velocity and density surveys employing particle image velocimetry (PIV), and interferometric techniques [1]. These techniques were all employed for trying to capture the well-known features associated with dynamic stall, and more specifically the complex flow behavior at the leading edge. In a more recent study, Pruski and Bowersox [10] studied the behavior of the leading-edge vortex using planar PIV and noted the growth of the vortex and its interaction with surrounding vorticity during the dynamic stall process. Their observations led to a modified physical description of the classical dynamic stall process, noting that the DSV appears as a coalescence of shear-layer vortices rather than a distinct singular vortex [10], a finding that prior researchers were unable to detect. Numerous computational studies since then have also appeared in the literature, attempting to capture the distinct flow features that have been documented within various experiments. Over a large range of flow conditions, many characteristics of deep dynamic stall have been established [1]. Namely, the formation of a DSV near the leading edge that convects along the airfoil, resulting in an overshoot of aerodynamic loads have been noted for a wide range of Reynolds numbers ($10^4 \leq Re \leq 10^6$). Although various distinct flow features have been realized and validated by many researchers both experimentally and computationally, the main question that remained open was the underlying viscous mechanisms from which these flow features develop [1], specifically regarding the physical process under which the DSV is formed, and the influence of the LSB

during the DSV formation. Although many studies noted the formation of a LSB, due to its small size, many experiments had been inconclusive on the role it plays in the development and behavior of the DSV, especially in its influence during the dynamic stall process. Although the behavior of the LSB in static stall has been well documented [11], Visbal and Garmann [1] were among the first to make a breakthrough with this question on the role of the LSB in dynamic stall. They studied the underlying mechanisms from which the DSV forms on a NACA 0012 blade section at a Reynolds number of 200,000 subject to a constant pitch rate motion. Using LES computations, they identified the effect of the LSB and its behavior during the dynamic stall process, finding that it was the initial trigger in the start of the dynamic stall process. Although its presence had been documented in previous studies, this LES case provided a detailed description of the unsteady boundary layer physics, which could not be identified through experimental methods. At a higher Reynolds number (10^6), Benton and Visbal [12] studied the turbulent separation induced leading-edge stall described by McCroskey et al. [6], concluding that the bursting of the LSB due to turbulent separation propagating upstream resulted in the development of a small leading edge vortex structure which rolled up the turbulent separated flow to develop the combined DSV. This was a mixed-type stall process that had not yet been visualized in literature but directly explained the origination of a DSV near the leading edge [12]. The behavior of the LSB documented by Visbal and Garmann [1] was similar to static analysis on a leading-edge LSB in 2D, by Pauley et al. [11]. As mentioned previously, despite extensive analytical, numerical, and experimental efforts, dynamic stall is not yet fully understood and characterized. This is due to its sensitivity to an array of factors, with the most important being the Reynolds number, wing geometry, and pitch rate, however the results of [1] and [12] have proven LES to be effective in studying the flow features that were elusive in experimental approaches.

This particular study aims to determine the feasibility of high fidelity DDES to study relevant flow physics with a much coarser spatial and temporal resolution in comparison with high fidelity LES. Not only will predictions of aerodynamic loads be discussed, but physics of

the dynamic stall vortex (DSV) will be studied to provide a concrete answer to whether complicated flow features can be realized from an industry oriented CFD approach and assess the computational and experimental findings researchers have observed regarding the flow features associated with dynamic stall. The emphasis will be to study the different stages during the dynamics stall process as a whole before diving into a deeper investigation of the leading-edge flow features.

1.3.3 Computational Fluid Dynamics

Recent progress in computational methods and the tremendous increase in computing power has made it possible to solve the full fluid governing equations for dynamic stall investigation and prediction in the design process. Although there did exist numerical methods for solving the unsteady Navier-Stokes equations, researchers in the late 20^{th} century lacked the accuracy and flow visualization tools that are equipped with many solvers today. Along with gathering accurate data on the dynamic stall process, researchers can get an accurate physical representation of the results generated from numerically solving the Navier-Stokes equations. Computational Fluid Dynamics (CFD) involves discretizing the non-linear Navier Stokes equations into a set of algebraic equations. Researchers highlighted the need for highly resolved simulations to capture the small scales associated with the laminar separation bubble and wall-bounded turbulence, making the LES approach very effective in the study of dynamic stall [12], since it ignores very small length scales and resolves those beyond a certain threshold. With this method still being computationally expensive, there are currently many researchers gravitating towards the use of computationally inexpensive models such as Reynolds Averages Navier-Stokes (RANS) and DDES. However, there still exists uncertainty in these CFD solvers since the Navier-Stokes equations are closed by assuming a turbulence model. The choice of the turbulence model has a significant effect on the final solution of computed pressure and velocity fields, bringing in an element of uncertainty.

1.3.4 Transition Modeling

Laminar-turbulent transition is a complex phenomenon that has a massive impact in the analysis of dynamic stall. There has been a tremendous amount of improvements in the past few decades with regards to an accurate prediction of transition and its addition to widely used CFD codes. These efforts have resulted in a wide variety of turbulence models that can be used for many applications, with reasonable accuracy and efficiency from a computational cost standpoint. Although there is a significant number of publications on this topic, there are several reasons to why this remains a loosely defined topic. This is related to the fact that transition occurs in different ways depending on the flow conditions. With flows relating to fixed-wing aircraft flight, transition is a direct result of flow instability, where the exponential growth of 2D disturbance waves leads to a nonlinear breakdown to turbulence [13]. Transition occurring due to Tollmein-Schlicting (TS) waves is referred to natural transition. For turbomachinery applications, bypass transition is the primary transition mechanism, where the transition process goes from the formation of TS waves directly to the development of turbulent spots prior to the breakdown to fully turbulent flow. Figure 3 gives a visual representation of the various transition mechanisms. The last, and most common mechanism is separation induced transition, which is caused through the laminar boundary layer separating under the influence of a large adverse pressure gradient. While all these different mechanisms have been widely studied, it remains a difficult task to include all the effects into a simple, yet versatile model.

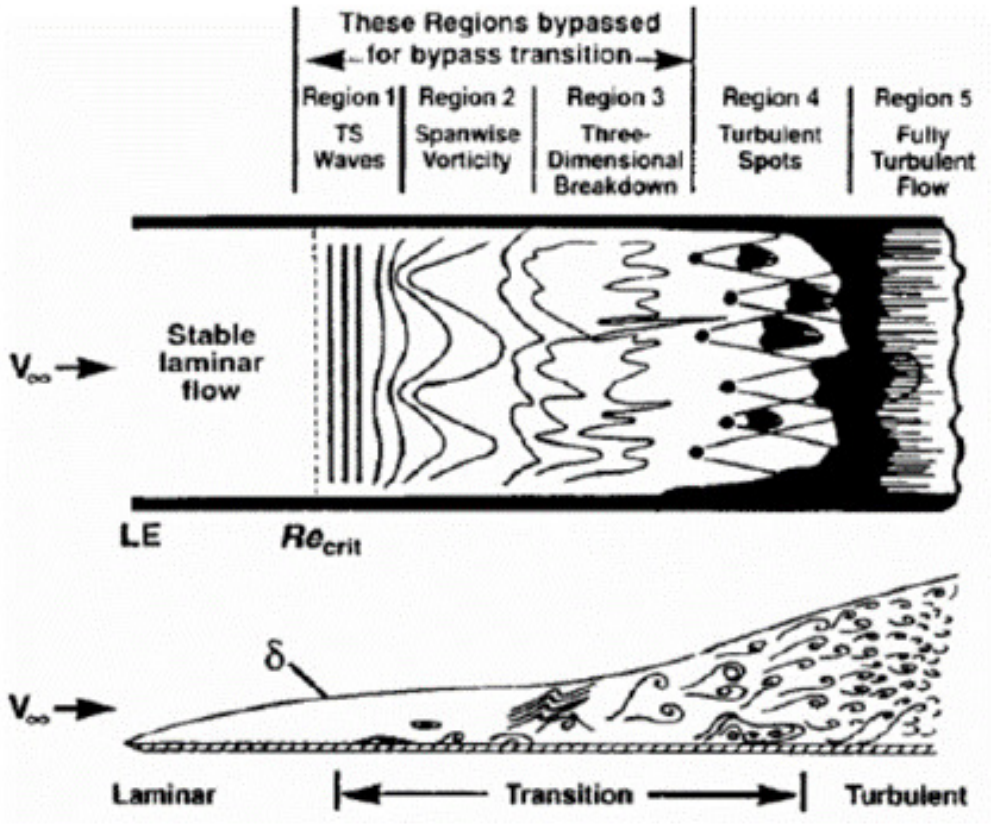

Figure 3: Different methods of laminar-turbulent transition [14].

Chapter 2

Problem Specification

2.1 Problem Description

In this paper a NACA 0012 airfoil section with a blunt trailing-edge is studied in detail. The three mesh resolutions studied are reported in Table 1. To prevent a sudden ramp-up motion, the pitch rate, $\dot{\alpha}$, is given by

$$\dot{\alpha}(t^*) = \psi_\circ^+(1 - e^{-4.6t^*/t_\circ}) \tag{2.1}$$

where $t^* = tU_\infty/c$ denotes the non-dimensional time, $t_\circ = 0.5$, and $\psi_\circ^+$ is 0.05. This allows the pitch rate to reach 99% of its asymptotic value, or $\psi_\circ^+$, fairly quickly ($t_\circ = 0.5$). Figure 4 shows a general schematic of the pitching motion applied. Although a constant pitch motion is more relevant to fixed-wing fighter aircraft and wind turbine blades, the underlying viscous flow physics is still applicable to rotorcraft environment. Based on studies done by Visbal and Garmann [1], a span of 10% chord was found to be a viable option for capturing 3 dimensional effects at a reasonable computational cost. Prior to the initial pitch up motion, a

well resolved static solution is first found. The boundary conditions are prescribed as follows: no-slip adiabatic condition on the airfoil surface, grid periodicity imposed in the chordwise direction at the trailing edge, and for keeping a nominal 2D configuration, spanwise periodic conditions are imposed. This essentially removes finite 3-dimensional effects such as the influence of tip vortices in this case study, but also allows for the study of spanwise features and effects within the flow. In regards to the temporal resolution, A small non-dimensional time step $\Delta t^* = 0.000256$ is utilized in this study. This correlates to 35,000 steps during the upstroke motion, and 1300 steps per angular degree of rotation. This small time step not only ensures numerical accuracy, but provides an adequate temporal resolution for capturing complex flow features. Furthermore, 30 sub-iterations are used for numerical convergence based on studies conducted by Liggett and Smith [15] on sufficient temporal resolutions of separated flows.

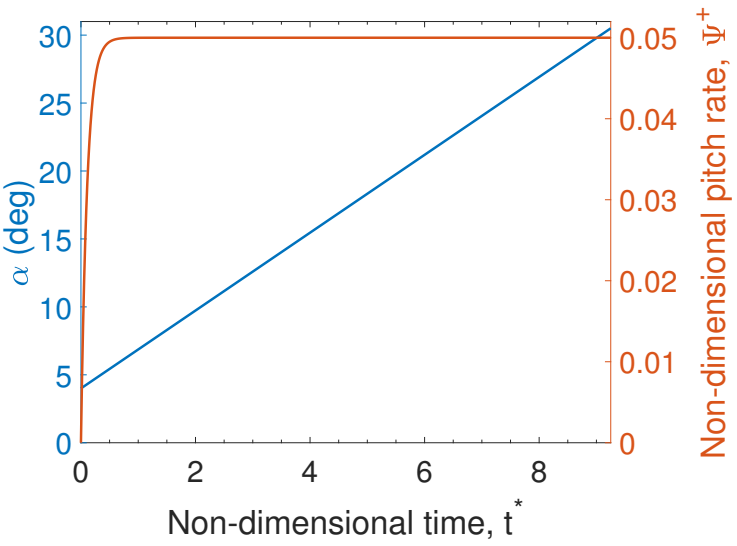

(a)

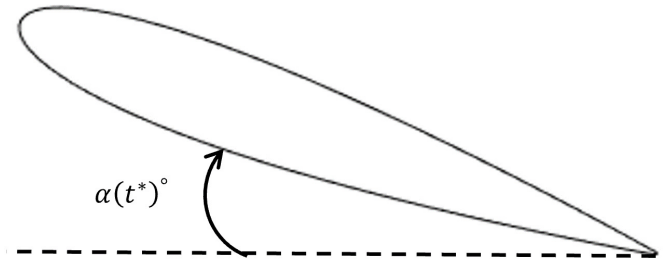

(b)

Figure 4: a) Prescribed pitching motion, and b) general schematic.

2.2 Grid Generation

The airfoil section is comprised of a single near-body curvilinear O-mesh. The NACA 0012 airfoil coordinates are imported into OVERGRID [16]. The modules HYPGEN, GRIDED, and SRAP, within the Chimera Grid Tools (CGT) package were used to generate the grids. CGT provides a graphical user interface and a unified environment for the visualization, processing, and diagnosis of the grid. The first 2D volume grid is generated through the use of HYPGEN, where a field grid is created from the NACA 0012 surface coordinates. The marching distance, initial and/or end spacings are user specified. The leading and trailing-edge chordwise spacings are kept at 0.02%c , where c denotes the chord length, to have a sufficient resolution for capturing the flow physics. Mesh smoothing parameters are kept at default values, a process that is standard when considering grids that are not overly complex [16]. After a 2D volume grid is generated, it is duplicated and concatenated in the spanwise direction to generate the 3D volume grid. The grid stretches 100 chords away from the surface, in accordance with [1]. It is replicated in the same manner for this study in order to make a fair comparison with LES results. Moreover, a majority of the grid points are concentrated within one chord length away from the airfoil surface, and 50 points are used in the far field, which provides a large grid stretching and dissipation of flow variables at the far-field boundary. Although the grid is stretched rapidly, the stretching ratio was maintained below 1.3 in accordance with OVERGRID best practices [16]. The grid resolutions represented as normalized wall units are found in Table 2. These represent computational step sizes calculated from the solution data. For all grids, the average y^+ calculated from the solution data is approximately 0.4 across the upper surface of the blade. This calculation of y^+ is done through an iterative process of adjusting flat plate approximations, and cross referencing with the solution data. The first grid point is placed within the boundary layer, approximately 5.19×10^{-5} meters from the airfoil surface. General schematics of the domain can be seen in Fig 5.

Table 1: Mesh Properties

Grid	Dimensions	N_{upper}/N_{lower}	$\Delta z/c$
1	$511 \times 100 \times 50$	350/150	0.002
2	$811 \times 200 \times 100$	600/200	0.001
3	$1349 \times 400 \times 100$	900/400	0.001

*Note: Dimensions are reported as (Chordwise $\times$ Normal $\times$ Spanwise). $\Delta z/c$ indicates the nominal spanwise spacing.

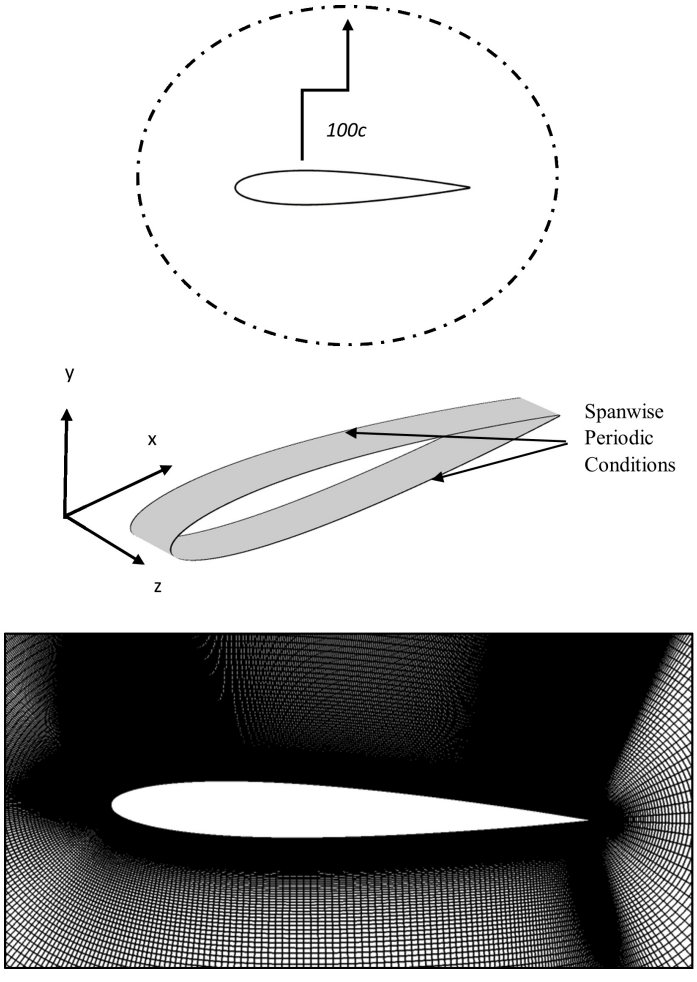

Figure 5: Overview of airfoil section mesh.

Table 2: Wall Units

Grid	Δx^+	Δy^+	Δz^+	$\overline{\Delta x^+}$	$\overline{\Delta y^+}$	$\overline{\Delta z^+}$
1	40.0	0.463	8.93	35.5	0.392	9.49
2	23.1	0.488	9.41	17.6	0.375	7.22
3	15.0	0.526	10.4	11.4	0.399	7.69

*Note: $\Delta x^+, \Delta y^+$, and Δz^+ indicate the grid spacing at $x/c = 0.8$. $\overline{\Delta x^+}, \overline{\Delta x^+}, \overline{\Delta x^+}$ indicate the grid spacings averaged across the airfoil upper surface.

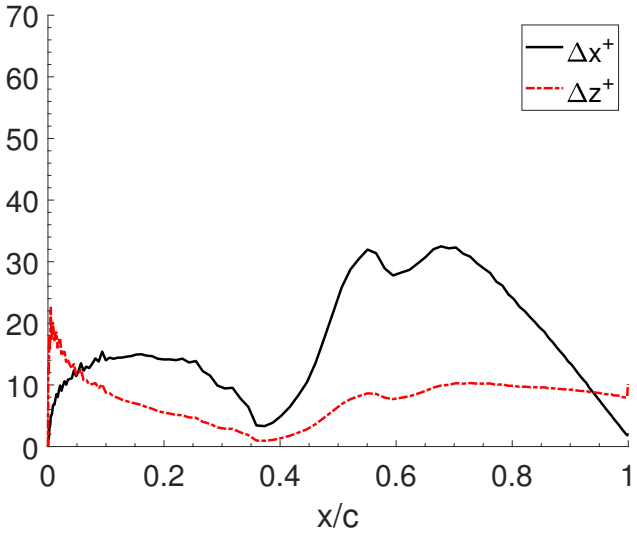

Figure 6: Streamwise (x) and spanwise (z) grid spacings on Grid 2.

Chapter 3

Numerical Procedure and Validation

3.1 OVERFLOW 2.3

The numerical integration of the unfiltered fluid transport equations is carried out using NASA's OVERFLOW 2.3 CFD code [17]. It is an implicit structured overset grid Navier-Stokes solver that is capable of computing time-accurate and steady state solutions with several options for temporal and spatial discretization. OVERFLOW was used to study 2D and 3D dynamic stall, [18–20], and various rotorcraft simulations, [21–23]. This code has a variety of turbulence and transition models available. The transition models used in this study are the following: (i) The correlation based two equation Langtry-Menter transition model [13], which is based on the year 2003 version of Menter's Shear Stress Transport (SST) model [24] with modifications to account for crossflow induced transition; (ii) the correlation based Medida-Baeder transition model [25], which is a reformulation of the Langtry-Menter Transition model to allow for integration with the Spalart-Allmaras (SA) Turbulence model, and (iii) Coder's Amplfication Factor Transport (AFT) model [26]. Furthermore, as previously stated, the fully turbulent SA model [27] is also used.

Governing Equations

The governing equations solved by OVERFLOW are outlined. The Navier-Stokes equations can be written in vector form with respect to a generalized coordinate system:

$$\frac{\partial \overrightarrow{q}}{\partial t} + \frac{\partial \overrightarrow{E}}{\partial \xi} + \frac{\partial \overrightarrow{F}}{\partial \nu} + \frac{\partial \overrightarrow{G}}{\partial \zeta} = 0 \tag{3.1}$$

where ξ, ν, and ζ represent the generalized coordinates. The fluxes in each direction are signified as $\overrightarrow{E}$, $\overrightarrow{F}$, and $\overrightarrow{G}$ The vector of conserved scalars is shown as:

$$\frac{\overrightarrow{q}}{V} = \begin{bmatrix} \rho \\ \rho u_1 \\ \rho u_2 \\ \rho u_3 \\ \rho e_\circ \end{bmatrix} \tag{3.2}$$

Here ρ, $\overrightarrow{u}$, and e are the unknown field variables of density, velocity, and total energy per unit mass, respectively, over the control volume V. These equations are linearized, and a pseudo-time term is added to allow for sub-iteration and faster iterative numerical schemes to be employed. The resulting system is given as the following:

$$\left[I + \frac{\Delta t}{(1+\theta)\Delta\tau} + \frac{\Delta t}{1+\theta}(\partial_\xi A + \partial_\eta B + \partial_\zeta C) \right] \Delta q^{n+1,m+1} = -\left[(q^{n+1,m} - q^n) - \frac{\theta}{1+\theta}\Delta q^n + \frac{\Delta t}{1+\theta} RHS^{n+1,m} \right] \tag{3.3}$$

For 2nd order temporal accuracy, $\theta = 1/2$ is used. The fluxes create the right-hand side

term

$$RHS = \frac{\partial \overrightarrow{E}}{\partial \kappa} + \frac{\partial \overrightarrow{F}}{\partial \nu} + \frac{\partial \overrightarrow{G}}{\partial \zeta} \tag{3.4}$$

Due to having five equations and six unknowns another equation is needed to close the system. The internal energy per unit mass e can be related to the temperature using the perfect gas assumption by

$$e_\circ = c_\nu T \tag{3.5}$$

where c_ν represents the specific heat at a constant volume. The internal energy per unit mass is related to the total energy per unit mass by

$$e = e_\circ + \frac{1}{2} u_\kappa u_\kappa \tag{3.6}$$

Finally, the system of equations is closed using the relation

$$P = \rho r T \tag{3.7}$$

The governing equations could be solved without further analysis using discretization techniques with appropriate integration and boundary conditions. However, this approach loses practicality as it would need a significant amount of computational resources to resolve even a small control volume. To account for this, turbulent length scales can be split into resolved and unresolved regions [28]. The resolved portions can be solved with a fine enough grid, while the unresolved portions can be modeled to reduce the computational cost. The

unresolved subgrid-scale stresses use an eddy viscosity model and are calculated from

$$\tau_{ij} = 2\mu_t \left(S_{ij} - \frac{1}{3}\frac{\partial u_\kappa}{\partial x_\kappa}\delta_{ij} \right) - \frac{2}{3}k\delta_{ij} \tag{3.8}$$

Several techniques can be used to solve for the turbulent eddy viscosity, μ_t, and the turbulent kinetic energy, k which can be modeled from the one equation Spalart Allmaras (SA) and the two equation Shear Stress Transport (SST) Turbulence Models [25].

Numerical Algorithm

Equation (3.3) has the general matrix form $Ax = b$. The first bracketed term is the left-hand side matrix A. The second bracketed term represents the vector b. Solving the system of equations described requires the inversion of the A matrix, which necessitates a large amount of computational time and memory. Various approximations are made to expedite the procedure. The factored form of eqn. (3.3) is given as the following

$$\begin{aligned}\left[I + \frac{\Delta t}{1+\theta}\partial_\xi A\right]\left[I + \frac{\Delta t}{1+\theta}\partial_\eta B\right]\left[I + \frac{\Delta t}{1+\theta}\partial_\zeta C\right]\Delta q^{n+1,m+1} \\ = -\left[(q^{n+1,m} - q^n) - \frac{\theta}{1+\theta}\Delta q^n + \frac{\Delta t}{1+\theta}RHS^{n+1,m}\right] + Error\end{aligned} \tag{3.9}$$

$$A = X_A \Lambda_A X_A^{-1} \tag{3.10}$$

$$B = X_B \Lambda_B X_B^{-1} \tag{3.11}$$

$$C = X_C \Lambda_C X_C^{-1} \tag{3.12}$$

$$X_A \left[I + \frac{\Delta t}{1+\theta} \partial_\xi \Lambda_A \right] \left[1 + \frac{\Delta}{1+\theta} \partial_\eta \Lambda_B \right] \left[I + \frac{\Delta t}{1+\theta} \partial_\zeta \Lambda_C \right] \Delta q^{n+1,m+1}$$
$$= - \left[(q^{n+1,m} - q^n) - \frac{\theta}{1+\theta} \Delta q^n + \frac{\Delta t}{1+\theta} RHS^{n+1,m} \right] + Error \quad (3.13)$$

Equation (3.13) is in scalar pentadiagonal matrix form. The inversion of this equation at each point can be done using extremely efficiently using the diagonal schemes within OVERFLOW [17].

Namelist Inputs

In this investigation, simulations are run with a fifth order central difference scheme for the flux algorithm and a diagonalized scalar pentadiagonal scheme for solution algorithm, both of which showed promising performance in 2D dynamic stall simulations [18]. Furthermore, a scalar dissipation scheme is employed with many smoothing parameters set to default by OVERFLOW standards. The primary means for convergence is based on the right-hand side (RHS) residual drop of the subiterations and maintaining close to a 2-order magnitude drop across each time step [29]. In the Reynolds number regime studied in this investigation, laminar separation occurs at the leading edge, hence three transition models are compared: SST Langtry-Menter ($\gamma - \tilde{R}e_{\theta t}$) model, SA Medida-Baeder ($\gamma - \tilde{R}e_{\theta t}$) model, and the SA James Coder Amplification Factor Transport (AFT) model.

3.2 AFT Transition Model

Evaluation of the turbulence production and destruction terms must not require any integration paths or global searches. In theory, it is possible to model the growth of instability frequencies using a transport equation, however, tracking multiple frequencies with the hope that one of them is the critical frequency requires a separate transport equation for each one, making this approach quickly lose its practicality. Drela and Giles developed the approximate envelope method, which provides an appealing alternative in the simplification of e^N theory to a single scalar variable [30]. This serves as the bases for the amplification factor transport equation. Furthermore, the secondary variable is the modified intermittency. The amplification factor is a measure based on a linear stability theory of how close a laminar boundary layer is to transition whereas the intermittency is a measure of the probability that a given point in space is located inside the turbulent region, that is the fraction of time that the flow is turbulent during transition [31]. The governing Partial Differential Equations (PDE) describing the evolution of the approximate envelope amplification factor and modified intermittency are given as the following

$$\frac{\partial \rho \tilde{n}}{\partial t} + \frac{\partial \rho u_i \tilde{n}}{\partial x_i} = \rho \Omega F_{crit} F_{growth} \frac{d\tilde{n}}{dRe_\theta} + \frac{\partial}{\partial x_i}\left((\mu + \sigma_n \mu_t) \frac{\partial \tilde{n}}{\partial x_i} \right) \tag{3.14}$$

$$\frac{\partial \rho \tilde{\gamma}}{\partial t} + \frac{\partial (\rho u_i \tilde{\gamma})}{\partial x_i} = c_1 \rho S F_{onset}(1 - exp(\tilde{\gamma})) - c_2 \rho \Omega F_{turb}(c_3 exp(\tilde{\gamma}) - 1) + \frac{\partial}{\partial x_i}(\mu + \sigma_n \mu_t) \frac{\partial \tilde{\gamma}}{\partial x_i} \tag{3.15}$$

Eqs. (3.14) and (3.15) are coupled to the SA equation for the working variable $\tilde{\nu}$

$$\frac{\partial \tilde{\nu}}{\partial t} + \frac{\partial (u_i \tilde{\nu})}{\partial x_i} = c_{b1} S \tilde{\nu} (1 - f_{t2}) - (c_{w1} f_w - \frac{c_{b1}}{\kappa^2} f_{t2}) \left(\frac{\tilde{\nu}}{d} \right)^2 \\ \frac{1}{\sigma} \left[\frac{\partial}{\partial x_i} (\nu + \tilde{\nu}) \frac{\partial \tilde{\nu}}{\partial x_i} + c_{b2} \frac{\partial \tilde{\nu}}{\partial x_i} \frac{\partial \tilde{\nu}}{\partial x_i} \right] \quad (3.16)$$

Through the modified f_{t2} term

$$f_{t2} = c_{t3}(1 - exp(\tilde{\gamma})$$

In the source terms of Eqs. (3.14) and (3.15) F_{crit} and $\frac{dn}{dRe_\theta}$ are functions of the displacement to momentum thickness ratio or integral shape factor H_{12}, itself a function of the local shape factor H_L

$$H_L = \frac{d^2}{\mu} \left[\Delta \rho \left(\overrightarrow{u} \frac{\Delta d}{d} \right) \frac{\Delta d}{d} \right] \quad (3.17)$$

where d is the wall distance and the first gradient factor acts as an indicator of pressure gradient from the freestream. H_L is limited within [-0.25,200] for numerical stability. F_{crit} toggles from 0 to 1 when the local vorticity Reynolds number

$$Re_\nu = \frac{\rho S d^2}{\mu + \mu_t} \quad (3.18)$$

reaches a critical threshold Re_{ν_θ} correlated to the transition momentum-thickness Reynolds number by a function of the integral shape factor H_{12}. The production term for the intermittency is activated by F_{onset}

$$F_{onset1} = min\left[\frac{\tilde{n}}{N_{crit}}, 2\right] \tag{3.19}$$

$$F_{onset2} = max\left[1 - \left(\frac{\mu_t}{3.5\mu}\right)^3, 0\right] \tag{3.20}$$

$$F_{onset} = max[F_{onset1} - F_{onset2}, 0] \tag{3.21}$$

and modulated by the laminar boundary-layer growth factor F_{turb}

In (3.14) the critical amplification number N_{crit} it is given by the Mack formula

$$N_{crit} = -8.43 - 2.4ln(\tau) \tag{3.22}$$

adapted for a high turbulence level with

$$\tau = 2.5tanh\left(\frac{Tu_\infty}{2.5}\right) \tag{3.23}$$

where Tu_∞ is the freestream turbulence intensity. $N_{crit} = 9$ has been shown to work well in a number of aerodynamics problems and it is therefore the default used here unless stated otherwise. At the inflow and farfield boundaries $\tilde{\nu}_\infty$ and $\tilde{\gamma}_\infty$ are set to zero, whereas extrapolation is used at the outflow and Neumann boundary conditions are applied at viscous walls [32]. An in-depth description and derivation of this transition model can be found in [33].

3.3 $\gamma - \tilde{Re}_{\theta_t}$ Transition Model

Correlation based transition modeling relies on a non-dimensional form of the boundary layer momentum thickness and its relation to the stability of the boundary layer. Similar to the e^N method, a fully laminar solution is initially presumed, and the momentum thickness Reynolds number is computed at all locations in the domain. The computed values are then compared to an empirical correlation to determine the location where transition is onset. Similarly with the issue described in the description of the AFT model, boundary layer parameters are non-local. The following equations outlined are with respect to Menter's Shear Stress Transport Model (SST). Rather than introducing a shape factor, components are localized through the relationship between vorticity Reynolds Number and momentum thickness Reynolds number [34].

$$\frac{\rho y^2}{\mu}\left|\frac{\partial u}{\partial y}\right| \tag{3.24}$$

Re_ν is related to Re_θ by the relation

$$Re_\theta = \frac{max(Re_\nu)}{2.193} \tag{3.25}$$

The $max(Re_\nu)$ corresponds to the maximum value the vorticity Reynolds number obtains in the plane normal to the surface. The denominator is chosen to be 2.193 such that for a Blasius profile $max(\frac{2.193 Re_\theta}{Re_\nu}) = 1$. A transport equation is used to distribute the empirical correlation throughout the flow field to enable the comparison between the local Reynolds and a localized onset value. This model defines the "transition onset momentum thickness Reynolds number" to serve as the onset criteria. Its transport equation is given by

$$\frac{\partial(\rho\tilde{Re}_{\theta t})}{\partial t} + \frac{\partial(\rho u_j \tilde{Re}_{\theta t})}{\partial x_j} = P_{\theta t} + \frac{\partial}{\partial x_j}\left[\sigma_{\theta t}(\mu + \mu_t)\frac{\partial \tilde{Re}_{\theta t}}{\partial x_j}\right] \tag{3.26}$$

The production term $P_{\theta t}$ is defined as

$$P_{\theta t} = c_{\theta t}\frac{\rho}{t}\left(Re_{\theta t} - \tilde{Re}_{\theta t}\right)(1 - F_{\theta t}) \tag{3.27}$$

The second transport equation of intermittency is given as

$$\frac{\partial(\rho\gamma)}{\partial t} + \frac{\partial(\rho u_j \gamma)}{\partial x_j} = P_\gamma - E_\gamma + \frac{\partial}{\partial x_j}\left[\left(\mu + \frac{\mu_t}{\sigma_f}\right)\right]\frac{\partial \gamma}{\partial x_j} \tag{3.28}$$

The production of intermittency attempts to simulate the transition process by progressively switching on the SST $k-\omega$ turbulence model. The value of intermittency in the freestream is set to 1 to accurately account for freestream turbulence decay rates, allowing the SST $\kappa - \omega$ model to function undisturbed outside the boundary layer. Once the onset criteria has been met, the intermittency is used to active the turbulence kinetic energy, k, through scaling the production term in the SST $k-\omega$ turbulence model

$$\frac{\partial(\rho k)}{\partial t} + \frac{\partial(\rho u_j k)}{\partial x_j} = \tilde{P}_\gamma - \tilde{E}_\gamma + \frac{\partial}{\partial x_j}\left[(\sigma_k + \mu)\frac{\partial k}{\partial x_j}\right] \tag{3.29}$$

where

$$\tilde{P}_k = \gamma_{eff} P_k \tag{3.30}$$

$$\tilde{D}_k = min[max(\gamma_{eff}, 0.1), 1.0]D_k \tag{3.31}$$

where γ_{eff} is an effective intermittency defined as a function of the transported intermittency and a laminar-separation criterion [34]. Implementation of the $\gamma - \tilde{Re}_{\theta_t}$ model with the SA turbulence model is relatively similar to the process described above, where the model retains the primary features of the original model by solving two scalar transport equations and using the local vorticity Reynolds number criterion and experimental correlations for the transition momentum thickness to predict the transition onset. A full list of the relevant equations relating to this SA counterpart of the $\gamma - \tilde{Re}_{\theta_t}$ model can be found in [25].

3.4 Static Validation

Static results are validated against XFOIL and LES results as a sanity check. These static cases are run continuously until there is stabilization of the aerodynamic loads and residual values. Figure 7 shows the surface pressure and skin friction coefficients with respect to the three grid resolutions for the SA AFT transition model. The CFD results are time and spanwise-averaged, and compared with XFOIL and LES [1] results. The purpose of this was to identify if the natural transition location and the overall surface pressure and skin friction coefficients are within acceptable margins. Prior to running the 3D dynamic cases, the mesh and numerical parameters are also validated via 2D RANS simulations on a 2D surface grid comprised of the same number of points in the chordwise (811) and normal (200) direction as Grid 2. Due to the lack of experimental data at $Re = 2 \times 10^5$, the CFD results are compared against experimental data by Hristov and Ansell [35] at a $M = 0.10$ and $Re = 1 \times 10^6$. The lift, drag, and pitching moment coefficient up until the static stall inception point can be seen in Fig. 8. Both the 2D and 3D static predictions show acceptable results for starting the 3D dynamic case.

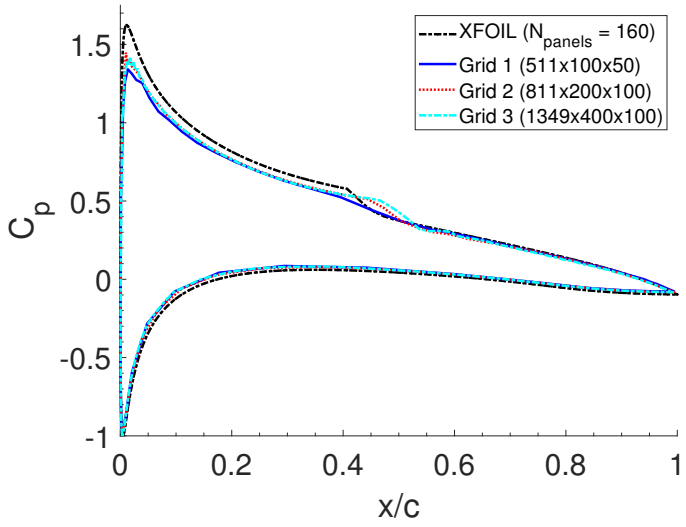

(a)

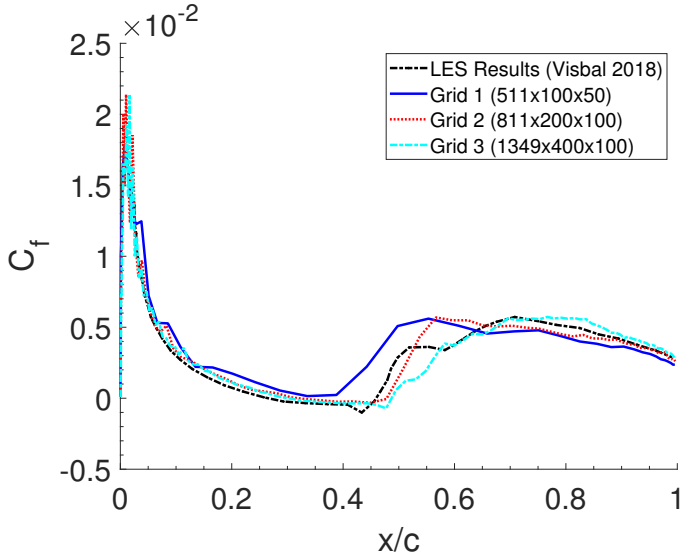

(b)

Figure 7: Grid resolution study on time and spanwise averaged a) C_p and b) C_f on 3D NACA 0012 airfoil section at $M = 0.10$, $Re = 2 \times 10^5$, and $\alpha = 4°$.

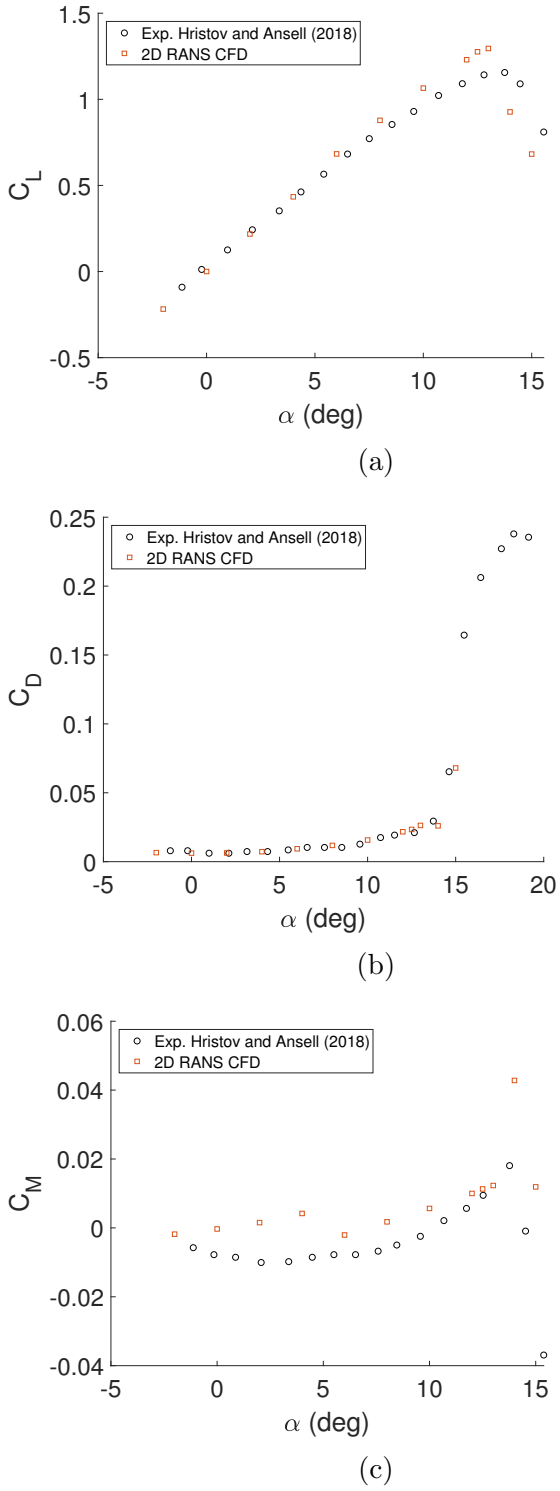

Figure 8: 2D RANS static validation of a) C_L, b) C_D, and c) C_M on a NACA 0012 airfoil at $M = 0.10$, $Re = 1 \times 10^6$.

Chapter 4

Dynamic Stall Results

4.1 Grid Resolution Study

This section presents an overall overview of the dynamic stall process, grid sensitivity, and validation with respect to the SA AFT transition model. Figure 9 shows the effect of all the grid resolutions during the upstroke phase. Similarly with the static case, validation is done through comparing predictions of the aerodynamic loads against the LES computations [1]. Grids 2 and 3 show relatively similar predictions in the converged aerodynamic loads and stall inception point during the dynamic stall process whereas Grid 1 shows an early onset of dynamic stall, which is an expected result considering the coarse grid configuration. The residual drop shown in Fig. 10 confirms numerical accuracy of the solution with all grid resolutions showing close to a two-order drop across each time step. For all cases the peak lift coefficient is underpredicted compared with LES, however, the predicted aerodynamic loads are within acceptable margins, permitting the study of flow physics with respect to Grid 2 ($811 \times 200 \times 100$) for the remainder of this study.

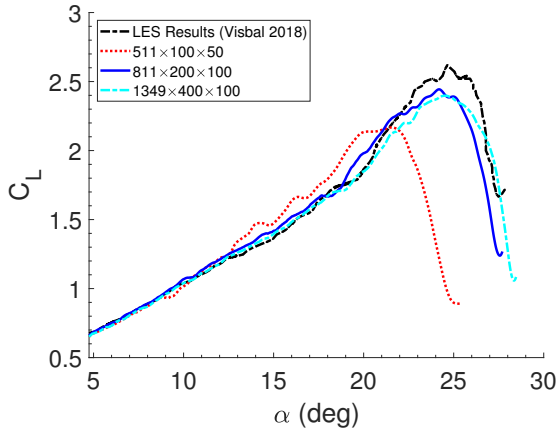

(a)

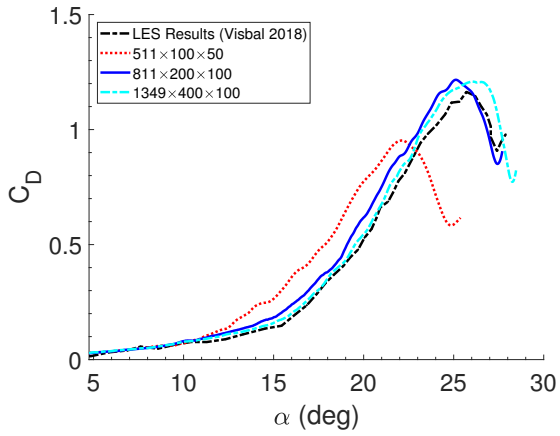

(b)

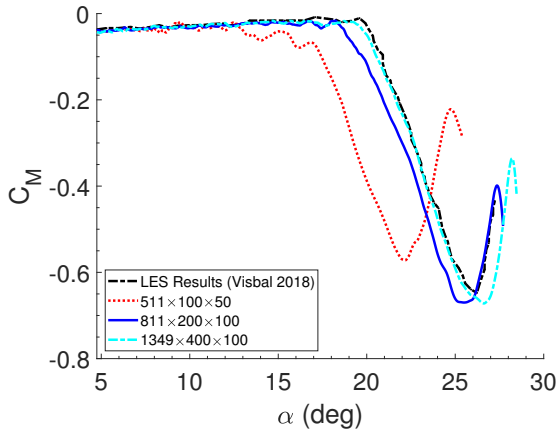

(c)

Figure 9: Grid resolution study comparison against LES [1] with 74M grid points ($1349 \times 410 \times 133$) for a) C_L, b) C_D, and c) C_M.

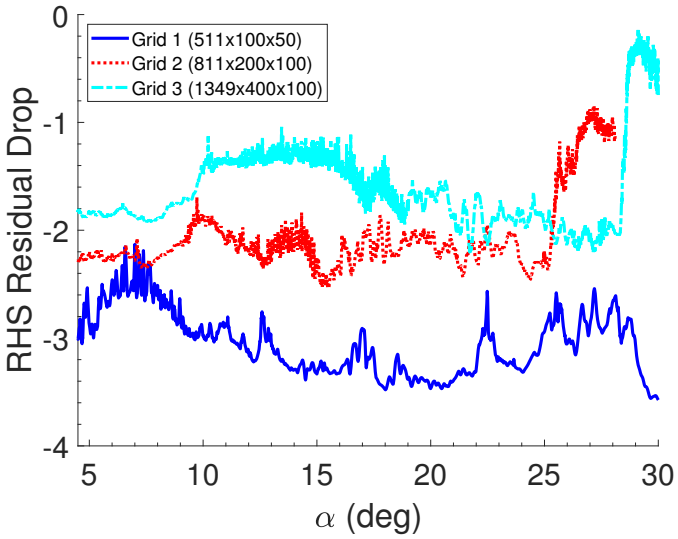

Figure 10: Residual drop for grids 1-3.

4.2 Dynamic Stall Stages

The dynamic stall process is broken down into various stages and studied more in depth within this section with respect to Grid 2 using the James Coder AFT transition model. These stages signify the important points during the dynamic stall process, similar to those described by McCroskey et al. [6] and Visbal and Garmann [1] which include an initial shear layer separation, loss of suction at the leading edge, and the subsequent formation and propagation of the DSV. It is important to note that in the following sections, many parameters of interest will be spanwise averaged and/or low pass filtered due to the extremely transient nature especially at high angles of attack. Analyzing one plane is sufficient for attached flows, however, averaging is more suitable to represent the averaged patterns of highly fluctuating flows. The different stages during the dynamic stall process can be seen in Fig. 11, along with their respective descriptions and flow topologies reported in Table 3. The spanwise averaged surface pressure and skin friction coefficients from stage 3 ($\alpha = 10.6°$) to stage 7 ($\alpha = 21.5°$) are seen in Figs. 12(a) and 12(b). As the angle of attack increases there is the gradual increase in maximum suction, however, as the flow begins to get closer to the point of the suction collapse, the flow near the leading edge starts becoming unstable, indicated by the oscillations in the pressure recovery region for the surface pressure and skin friction coefficients. This is in line with the findings of Pauley et al. [11] who found on 2D static stall experiments that for stronger adverse pressure gradients corresponding to increased suction, the separated region lengthened and small oscillations developed in the skin friction. The two distinct spikes in the surface pressure at stage 4 ($\alpha = 15.2°$) is due to the unsteadiness of the within the flow causing nearly two reattachment point of the boundary layer just downstream of the LSB before full pressure recovery. This occurs just prior to suction collapse as the adverse pressure gradient becomes too strong for the boundary layer to reattach smoothly.

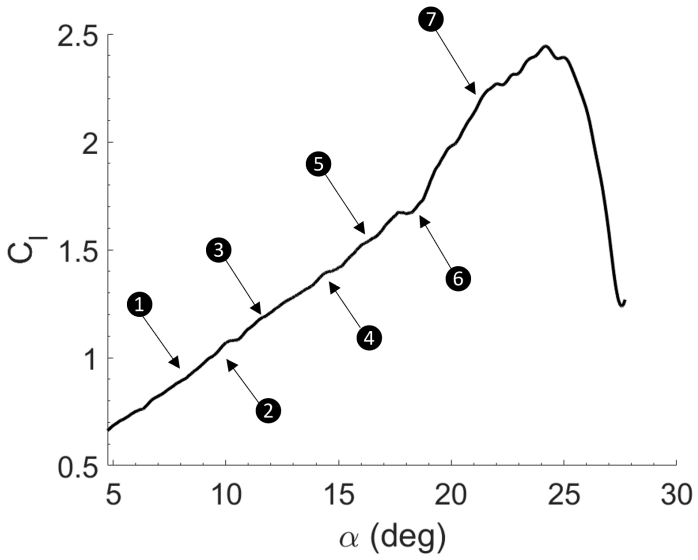

Figure 11: Various stages of dynamic stall (Grid 2).

Table 3: Dynamic Stall Stages

Stage	Flow Topology
1 ($\alpha = 8°$)	Boundary layer transition point is propagating upstream.
2 ($\alpha = 10.6°$)	A laminar separation bubble forming at the leading edge with initial shear layer separation and subsequent reattachment as a turbulent boundary layer.
3 ($\alpha = 12.9°$)	Increase in suction at the leading-edge and reattachment of turbulent boundary slightly further downstream than the previous stage. Gradual thickening of the boundary layer over the entire blade section.
4 ($\alpha = 15.2°$)	Suction still increasing at the leading edge, however adverse pressure gradient begins to have a more pronounced effect on the separation bubble, as instabilities begin to settle in, resulting in two reattachment branches of the boundary layer.
5 ($\alpha = 16.9°$)	Suction is lost at the leading edge as the laminar separation bubble collapses due to the strong adverse pressure gradient, causing a large region of unsteadiness at the leading-edge. Lift is still increasing linearly.
6 ($\alpha = 18.6°$)	The separated shear layer following the bubble collapse begins to roll up into a dynamic stall vortex. Significant increase in the $C_l - \alpha$ slope due to DSV formation.
7 ($\alpha = 21.5°$)	Dynamic stall vortex is fully formed and begins is propagating downstream, up until roughly 50% chord length where it detaches from the surface.

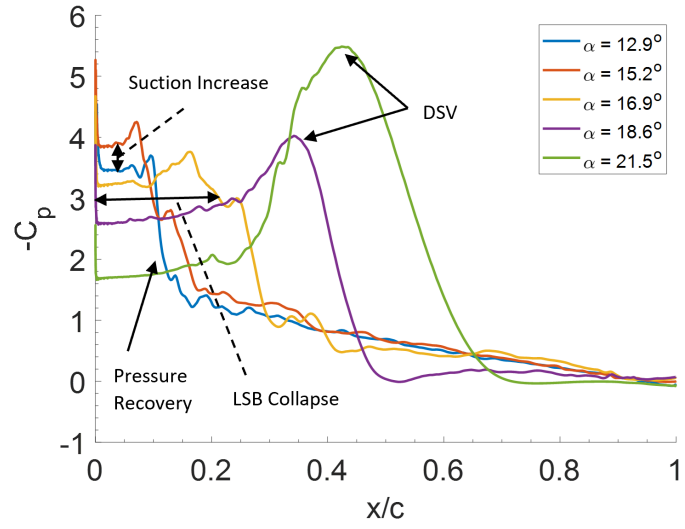

(a)

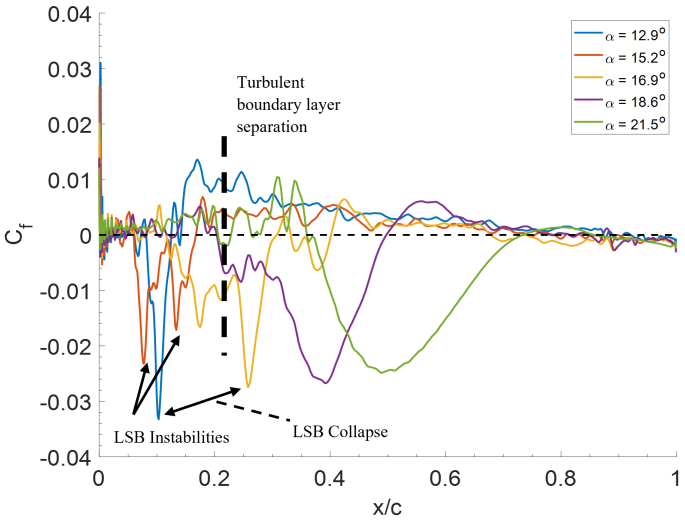

(b)

Figure 12: Spanwise-averaged a) C_p, and b) C_f during different stages in the dynamic stall process.

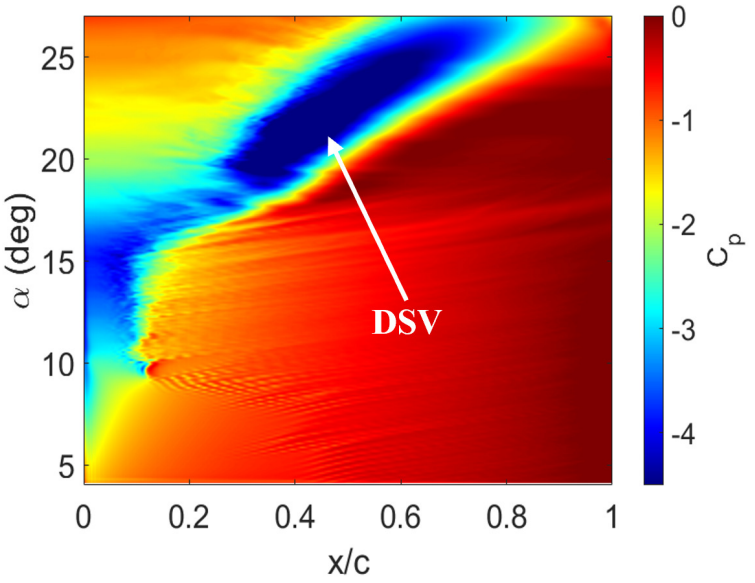

(a)

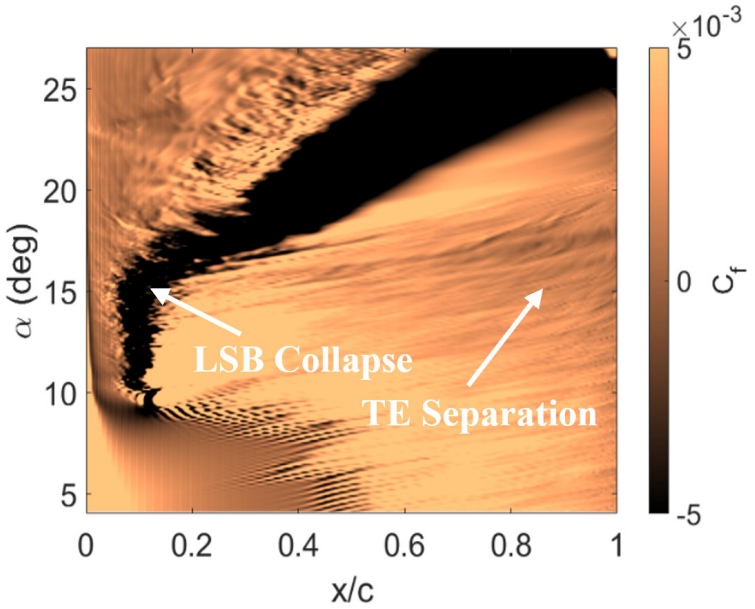

(b)

Figure 13: Spanwise-averaged contours of a) C_p and b) C_f during the dynamic stall process.

The contours of the surface pressure and skin friction can also be seen in Figs. 13(a) and (b) respectively throughout the duration of the dynamic stall process. The surface pressure contour in Fig. 13(a) shows the clear formation of the LSB and the propagation of the DSV. More interestingly, the contour of skin friction, shown in Fig. 13(b), indicates that this stall

process is related with "pressure gradient bubble bursting" leading-edge stall rather than "turbulent leading-edge" stall caused by the rapid upstream propagation of the reverse flow through the trailing edge. It can be seen that the reversed flow, indicated by the negative regions of skin friction near the trailing edge, does not propagate upstream throughout the duration of the prescribed motion. While some of the overall aspects regarding the dynamic stall have been discussed, the remainder of the sections will cover the flow physics more in depth throughout the various stages described.

4.3 General Flow Physics

The approximate transition location is predicted through the production of turbulent kinetic energy (TKE) within the boundary layer. The dashed line in Fig. 14 represents the spanwise averaged TKE from which approximations of the transition location are computed.

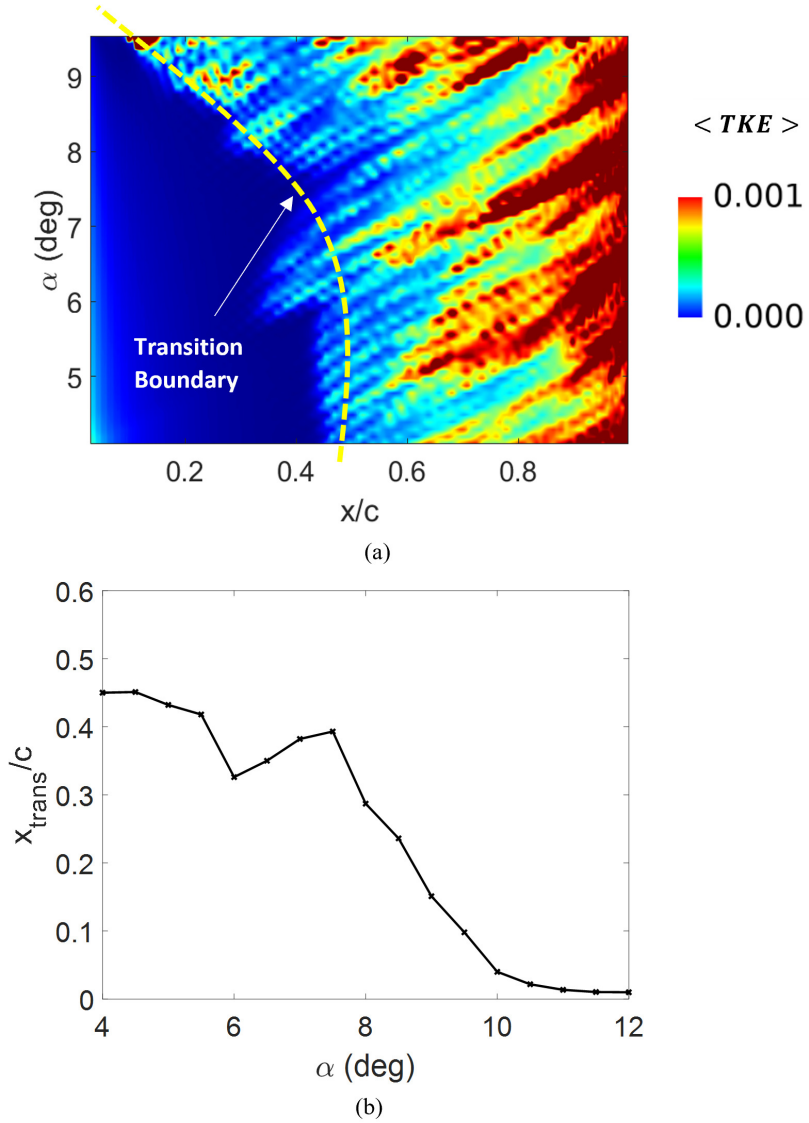

Figure 14: a) Contour of spanwise-averaged TKE production, and b) approximate transition location as a function of angle of attack.

The upstream propagation of the transition point has been documented by many researchers studying this phenomenon at low Reynolds numbers, including Gupta and Ansell [36], as well as Mulleners and Raffel [37], who performed experimental studies of dynamic stall at transitional Reynolds numbers. Figure 15 shows the vorticity magnitude during the various stages described above during the unsteady pitch up motion. From stage 1 ($\alpha = 8°$), transition can be seen through the small vortices present within the boundary layer as the transition point propagates upstream. Moreover, in the earlier stages, the formation and presence of a LSB can be seen through the vorticity magnitude production at the leading edge. This presence of the LSB is clearer from predictions of the surface pressure coefficient shown in Fig. 13(a) where there is a distinct pressure plateau at the leading-edge followed by a rapid recovery region, indicating turbulent reattachment of the boundary layer. As the angle of incidence increases there is a gradual increase in the boundary layer thickness that can be seen in Figs. 15(b)-(e). In Fig. 15(f) the presence of an initial trailing edge vortex (TEV) is seen through the rapid spatial growth in vorticity production towards the trailing edge. Even in the presence of vorticity production at the trailing edge, the overall external flow is not greatly deviated as the lift force continues to increase linearly. This is opposite to its counter-part static stall, where flow reversal usually provokes a massive flow separation followed by a drastic loss in lift and increase in drag [37]. Up until Fig. 15(d) there still exists suction at the leading edge, however as it is seen in the predicted pressure and skin friction contours, the instabilities begin settling in which eventually cause the collapse of the bubble due to the large adverse pressure gradient induced at higher angles of attack, which can be seen in from Figs. 15(d)-(e) through the sudden decrease in vorticity magnitude at the leading edge. This is the initial trigger for the further events correlated with the dynamic stall process. Following the collapse of the LSB, the separated shear layer beings to roll up into a DSV. Further details regarding the shear layer roll up and DSV formation will be discussed in subsequent sections. The suction collapse and successive formation of the DSV is indicated in the C_l, α curve in Fig. 11 through the sudden increase in the slope of the lift

coefficient beyond the linear region at approximately $\alpha = 18.6°$. This sudden change of the lift-curve slope was also documented by McCroskey [5], as well as Visbal and Garmann [1]. The nature of the DSV rotation results in entrainment of outer flow into the boundary layer near the point where the DSV is still attached to the surface [1]. This results in a strong reverse flow region under the DSV, indicated by the strong signature of vorticity magnitude seen close to mid-chord in Fig. 15(f). While the dynamic stall vortex continues to take up vorticity, counter-rotating vortices emerge near the airfoil's surface as a result of increasingly strong interactions between the DSV and the reversed flow due to entrainment, a feature that was experimentally captured and described by Mulleners and Raffel [37]. The rotating DSV pushes the counter rotating structures towards the leading edge, thereby forcing itself to detach; a process that is known as vortex-induced separation [37]. In the latter stages close to the stall point, there is the presence of longitudinal vortex sheets downstream of the DSV indicated by the distinct streaks in the vorticity magnitude close to the airfoil surface beyond the DSV, which were also noted by Visbal and Garmann [1]. At stage 7 ($\alpha = 21.5°$), the blade section is getting closer to the point of lift stall, as the DSV is still propagating downstream. Stall is onset just after Fig. 15(h) when the DSV is shed from the airfoil surface. The overall sequence of the events described lies in parallel to observations by Visbal and Garmann [1], McCroskey et al. [6], Shih et al. [9], and Carr et al. [38].

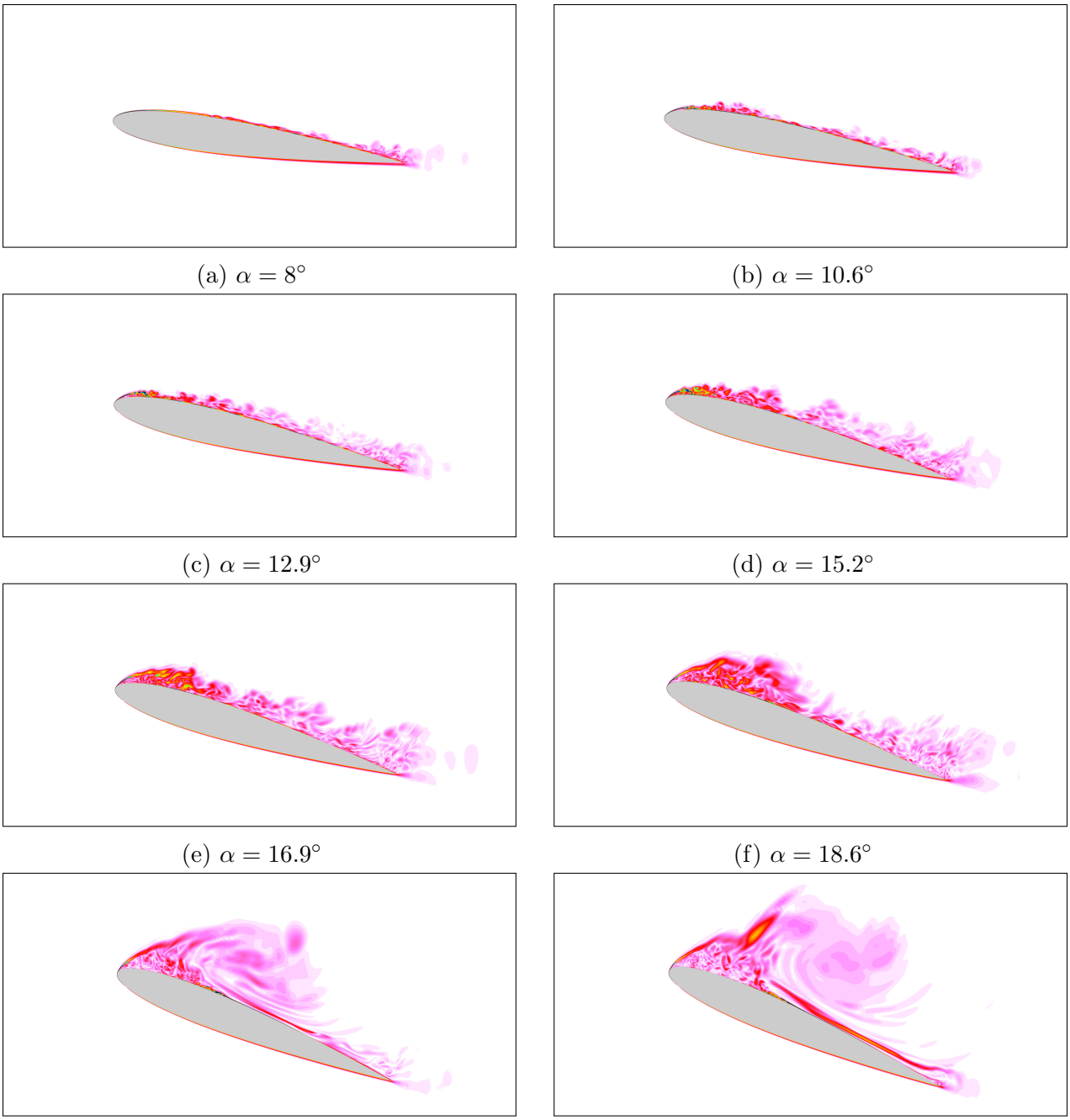

(a) $\alpha = 8°$ (b) $\alpha = 10.6°$

(c) $\alpha = 12.9°$ (d) $\alpha = 15.2°$

(e) $\alpha = 16.9°$ (f) $\alpha = 18.6°$

(g) $\alpha = 21.5°$ (h) $\alpha = 23.2°$

Figure 15: Instantaneous (midplane) contours of vorticty magnitude.

Figure 16 shows the time histories of the instantaneous (C_p), spanwise-averaged ($< C_p >$), and low-pass-filtered ($< C_p >_{lpf}$) surface pressure, C_p, and near-wall velocity, u_{nw} at the chordwise location $x/c = 0.15$. The instantaneous data across the airfoil surface is sampled every 125 time steps, correlating to every 0.1^o of rotation. This data is first spanwise-averaged, and then run through low-pass-filter to attenuate high frequency oscillations. As expected, the flow remains relatively parallel at low angles of attack with no real distinctive differences in instantaneous, spanwise-averaged, and low pass filtered pressure and velocity. The relative unsteadiness of the flow phenomena can be seen through the large spikes in both these flow variables just after the occurrence of transition and the formation of the LSB. Figure 16(a) depicts transition through the kink in the low pass filtered surface pressure near $\alpha = 8^\circ$, and similarly in Fig. 16(b), through the jump in the near wall velocity. The collapse of suction can be seen around $\alpha = 16^\circ$ where there exists a sudden increase in pressure.

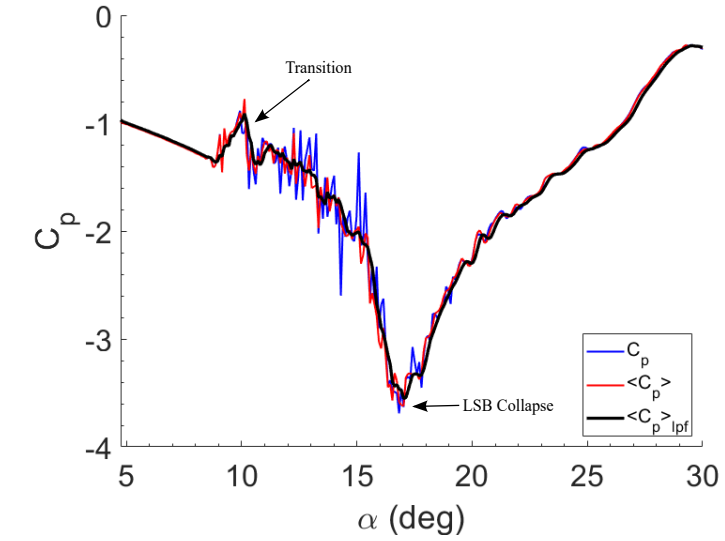

(a)

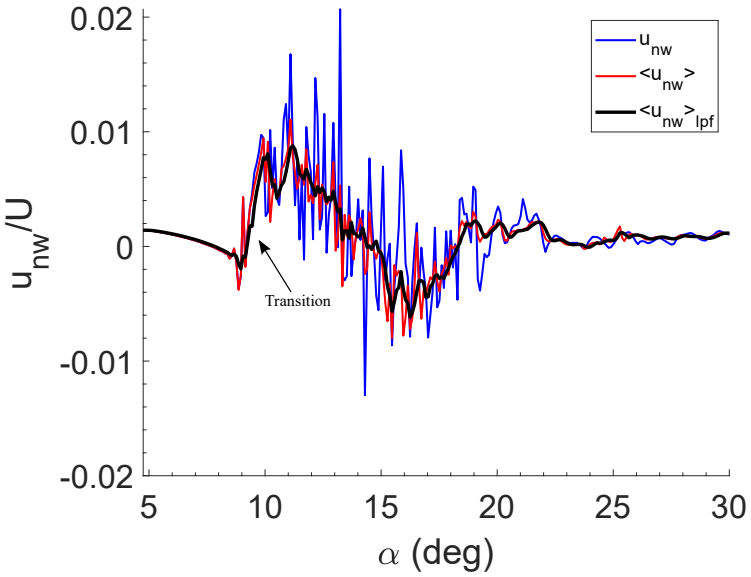

(b)

Figure 16: Represenations of instaneous, spanwise-averaged, and low-pass-filtered a) C_p, and b) u_{nw} at $x/c = 0.15$.

The iso-surfaces of Q-criterion, or the measure of swirling strength, shown in Fig. 17 depict the 3 dimensionality of this flow. The periodic shedding of coherent structures can be seen in Fig. 17(a), which lies in agreement with the findings of Kurelek et al. [39] who found that amplifications in the LSB generated on a NACA 0018 at a low Reynolds number caused the separated shear layer to roll up into coherent vortices that are shed from the leading edge. It can be noted downstream in Fig. 17(a), that these vortices deform rapidly and breakdown into fine scale turbulent structures past the reattachment point where there exists a fully turbulent boundary layer. In Fig. 17(c) the entrainment of outer fluid just beyond the DSV can be seen through a distinct quiescent region mid-chord, in between the DSV and initial trailing edge vortex (TEV), where the presence of strong vortices is not captured. The DSV dynamics can be recognized as the leading-edge separated shear layer transitions from detachment close to the airfoil surface to full separation far from the airfoil surface, a feature also noted by Visbal and Garmann [1].

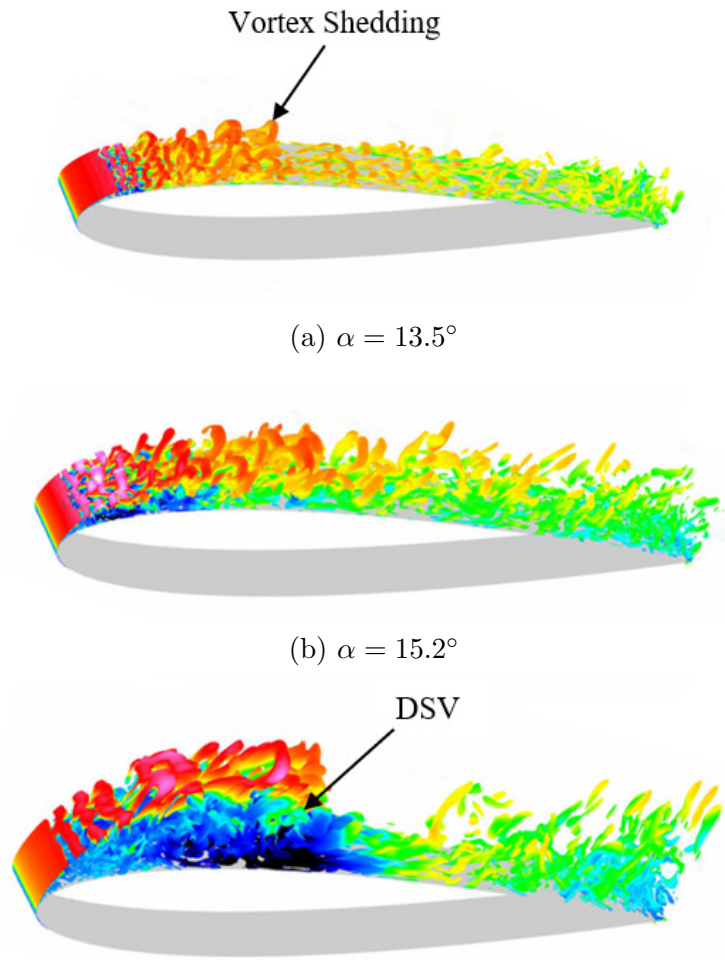

(a) $\alpha = 13.5°$

(b) $\alpha = 15.2°$

(c) $\alpha = 18.6°$

Figure 17: Iso-surfaces of Q-criterion = 25 colored by streamwise velocity.

The overall behavior of the unsteady flow is also shown in Fig. 18 by the instantaneous contours of TKE. Figures 18(b)-(d) show the gradual thickness of the turbulent boundary layer, which was also identified in the vorticity magnitude contours from Fig. 15. The breakdown of suction at the leading-edge can be seen by the rapid decrease of TKE production at the leading edge by Fig. 18(d). In this stage, the shear layer begins to roll up into a DSV, which is seen in Fig. 18(d) as the separated shear layer shows interaction with the unsteady region just after the LSB collapse that eventually leads up to the DSV formation. More interestingly, the distinct pockets of TKE during the formation of the DSV in Figs. 18(d)-(e) agree with the findings of Mulleners and Raffel [37] as well as Pruski and Bowersox [10], who found that the DSV consists of a combination of rolled-up shear layer and remnants of several vortices induced by the instability of the shear layer at the leading edge. The early stages of vortex induced separation of the DSV can be clearly visualized from Figs. 18(f) and (g), where there is the transition of strong TKE production at the surface, to a more separated boundary layer, indicating the interaction between the DSV and the reversed flow just below the DSV, which causes the vortex induced detachment.

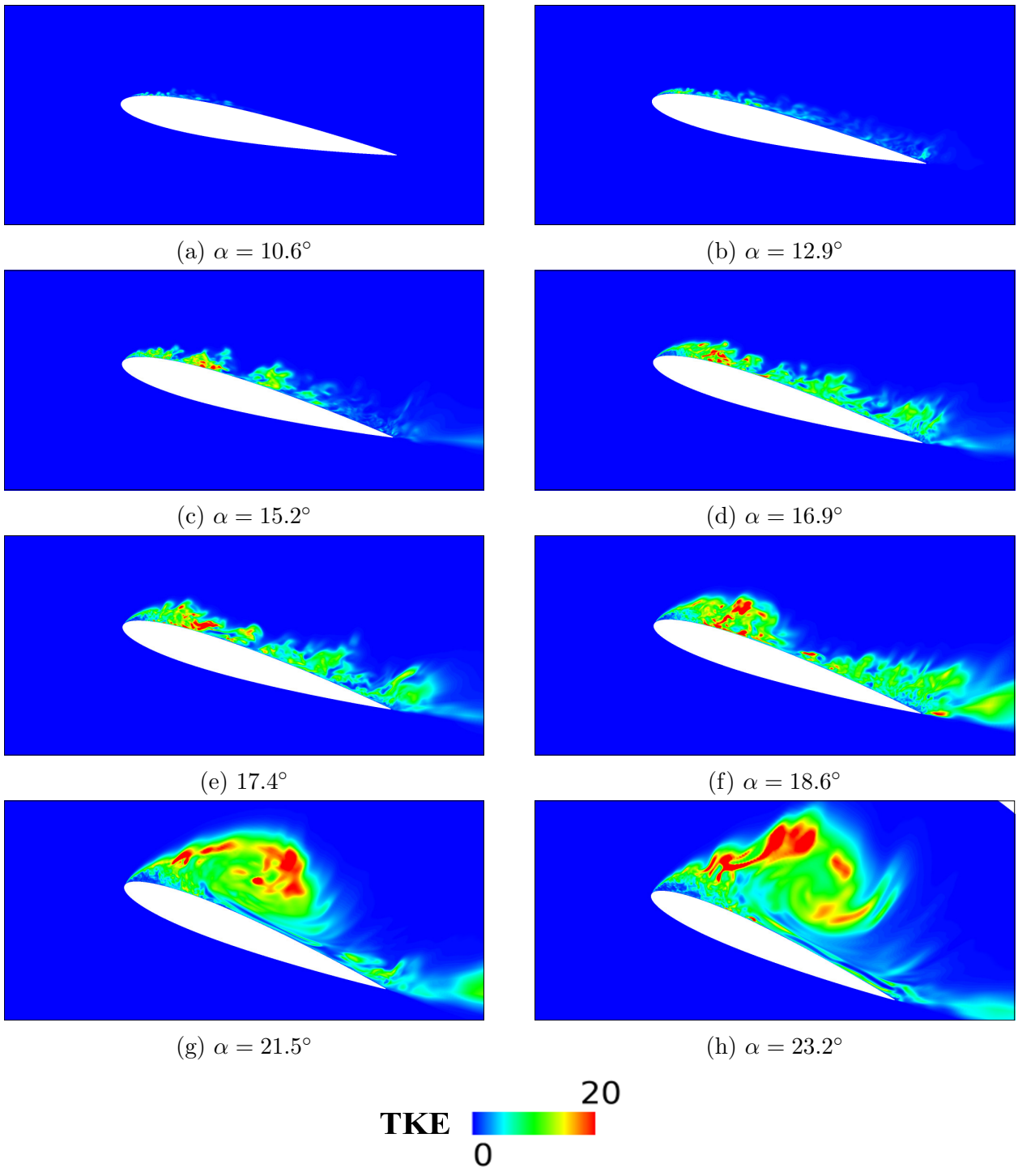

Figure 18: Instantaneous (midplane) TKE across various dynamic stall stages.

Figure 19 shows the time history of the dynamic stall process at a variety of chordwise stations. Figure 19(a) portrays the formation and collapse of the LSB. Stations $x/c = 0.1$ and 0.15 are of great interest as they capture the transition to turbulent flow through the respective peaks in the spanwise averaged pressure coefficient, in parallel with computations by Visbal and Garmann [1]. In Fig. 19(b), the presence of the DSV is seen through the negative peaks in the pressure. The gradual strength of the DSV can be seen up until roughly 40% chord length, in which case, the DSV starts to shed from the surface of the airfoil. This point is characterized by the peak lift coefficient in Fig. 11, just prior to the onset of stall. This point of the DSV reaching its maximum strength lies in parallel with observations reported by McCroskey et al. [6] in their study of turbulent leading-edge stall, where the vortex detaches close to mid-chord, and lift stall ensues. The detachment of the DSV is the reason for the weaker signatures of the surface pressure at downstream locations past the stall angle.

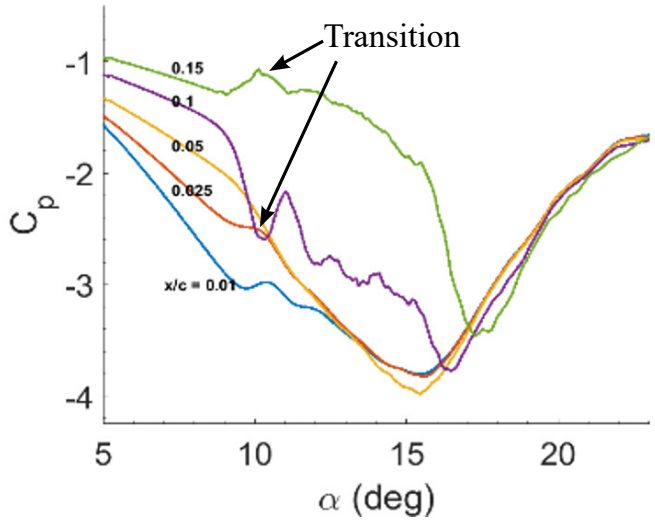

(a)

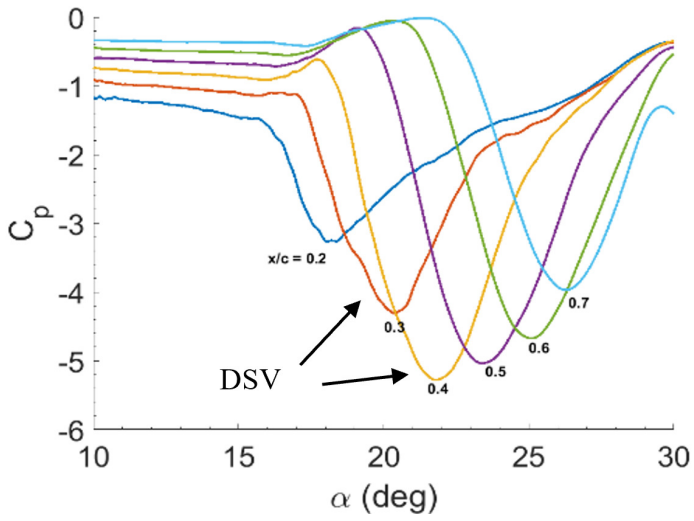

(b)

Figure 19: Time history of low-pass-filtered C_p representing a) LSB collapse and b) DSV formation and propagation at various chordwise stations.

4.4 Leading-Edge Flow Features

This section will investigate the unsteady flow physics at the leading edge in more detail, focusing on the process of DSV formation. The existence of a LSB within this flow regime is very well known and has been documented by Visbal and Garmann [1], McCroskey et al. [6], Carr [7], and McCroskey et al. [38], and others. Even though its highly unsteady nature makes it difficult to fully grasp, there are some general characteristics which have been identified regarding the influence of the LSB on the dynamic stall process. For example, at high Reynolds numbers, it has been documented that the bursting of the LSB is induced more so by the upstream propagation of the reverse flow within the boundary layer, starting from the trailing edge [12]. At lower Reynolds numbers, the LSB collapse has been documented as a result of pressure gradient-induced bursting. Initial experiments by Ham first linked the formation of the DSV to the LSB prior to airfoil stall [8], documenting it on a NACA 0012 airfoil at a Reynolds number of $300,000$. Ham along with a variety of other researchers: Chandraeskhara, Carr, and Wilder [40], Lee and Gerontakos [41], Martin et al. [42], all documented the presence of a LSB at the leading edge prior to stall but couldn't clearly identify the bursting process and the effect it had on the overall DSV formation/dynamic stall process. Many studies showed high sensitivity of dynamic stall behavior to the Reynolds number, hence accurate conclusions couldn't be made to the influence of solely the LSB. As discussed previously, McCroskey et al. [6] did a more extensive study based on the findings during the late 20th century and identified different forms of which dynamic stall is onset. For lower speed applications, the stall process has been documented by pressure-gradient induced bursting of the laminar separation bubble. They stated the laminar separation bubble can remain small, but the turbulent flow over the bubble can reach a state where the reattachment is no longer possible, causing a breakdown of the bubble, and producing "leading-edge bubble-bursting stall" [6]. This section will investigate the feasibility of DDES in terms of capturing the overall leading-edge boundary layer behavior.

Figure 20 shows the spanwise variation in the streamwise velocity at different stages during the dynamic stall process. From Fig. 20(a), the clear onset of the LSB can be seen through concentrated region of reversed flow along the span. The consequent bursting of the LSB and the formation of a DSV appear on the wider stretched velocity contours. The presence of the strong region of a reversed flow below the DSV is consistent with the findings of Gupta and Ansell [36] who observed the region of reversed flow under the DSV, connecting it with the entrainment of outer flow into the boundary layer. Moreover, this is consistent with Fig. 15(f) and 18(f), where this region shows a localized region of a high vorticity magnitude and a high TKE production.

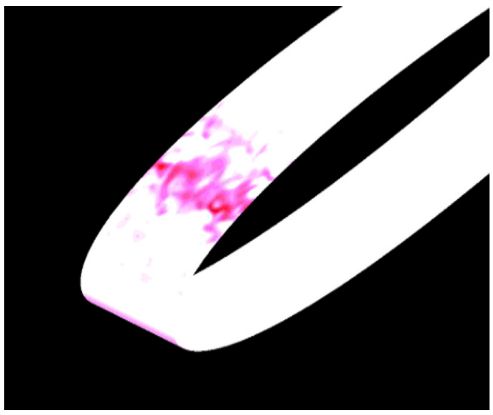

(a) α = 10.6°

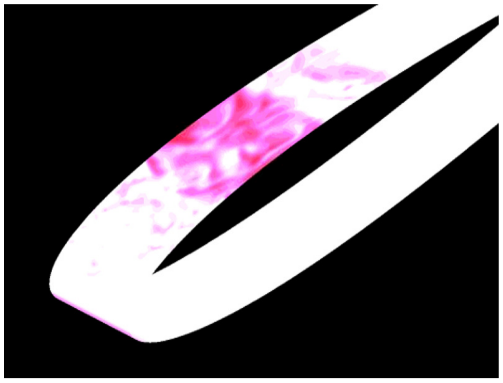

(b) α = 16.9°

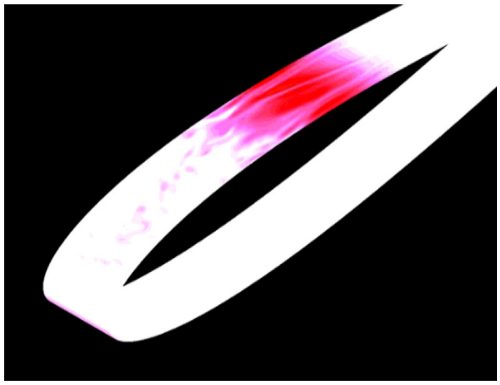

(c) α = 18.6°

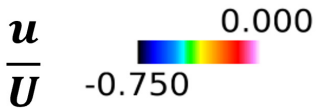

Figure 20: Spanwise variation of instantaneous streamwise velocity.

Figure 21 shows the behavior of the LSB at the leading edge through representation of the reversed flow. Here, the formation of the bubble is seen through the presence of slightly reversed flow at the leading edge. There is a gradual increase in reversed flow within this region up until Fig. 21(b) where there is a clear visual of the LSB itself. Prior to the collapse of the LSB, the upstream propagation of the bubble is apparent from Figs. 21(c)-(d), where the reversed flow propagates towards the leading edge between $\alpha = 12.9°$ and $\alpha = 13.5°$. The profile at $\alpha = 15.2°$ suggests the claims previously mentioned of instabilities starting to settle in the flow. The collapse of the LSB is captured at $\alpha = 16.9°$, where there no longer exists a concentrated region of reversed flow at the leading edge, and there is the presence of a more chaotic velocity distribution. Previous predictions by Visbal and Garmann [1] with a denser grid configuration showed a maximum contraction and suction peak at 15.2°, followed by the abrupt collapse of the bubble. From this current study, although there is a contraction of the bubble seen from $\alpha = 12.9°$ - $\alpha = 13.5°$, prior to the complete loss of suction, it seems the bubble is contracting and expanding continuously prior to collapse. In Fig. 21(f), shows the initial stages of the DSV formation can be seen through the large unsteady reverse flow region present. The reverse flow profiles indicates that although the separation bubble itself doesn't generate stall directly, it does have a significant influence on the overall stall process, as upon collapse, there is the distribution of unsteady flow downstream that eventually leads to the formation of a DSV. Moreover, during these earlier stages, there is not a significant indication of strong reversed flow near the trailing edge, indicating that this type of stall is in parallel with Visbal and Garmann [1], McCroskey et al. [6], and Gupta and Ansell's [36] description of abrupt leading-edge stall induced through a strong adverse pressure gradient bursting the LSB rather than rapid propagation of reversed flow upstream meeting the LSB.

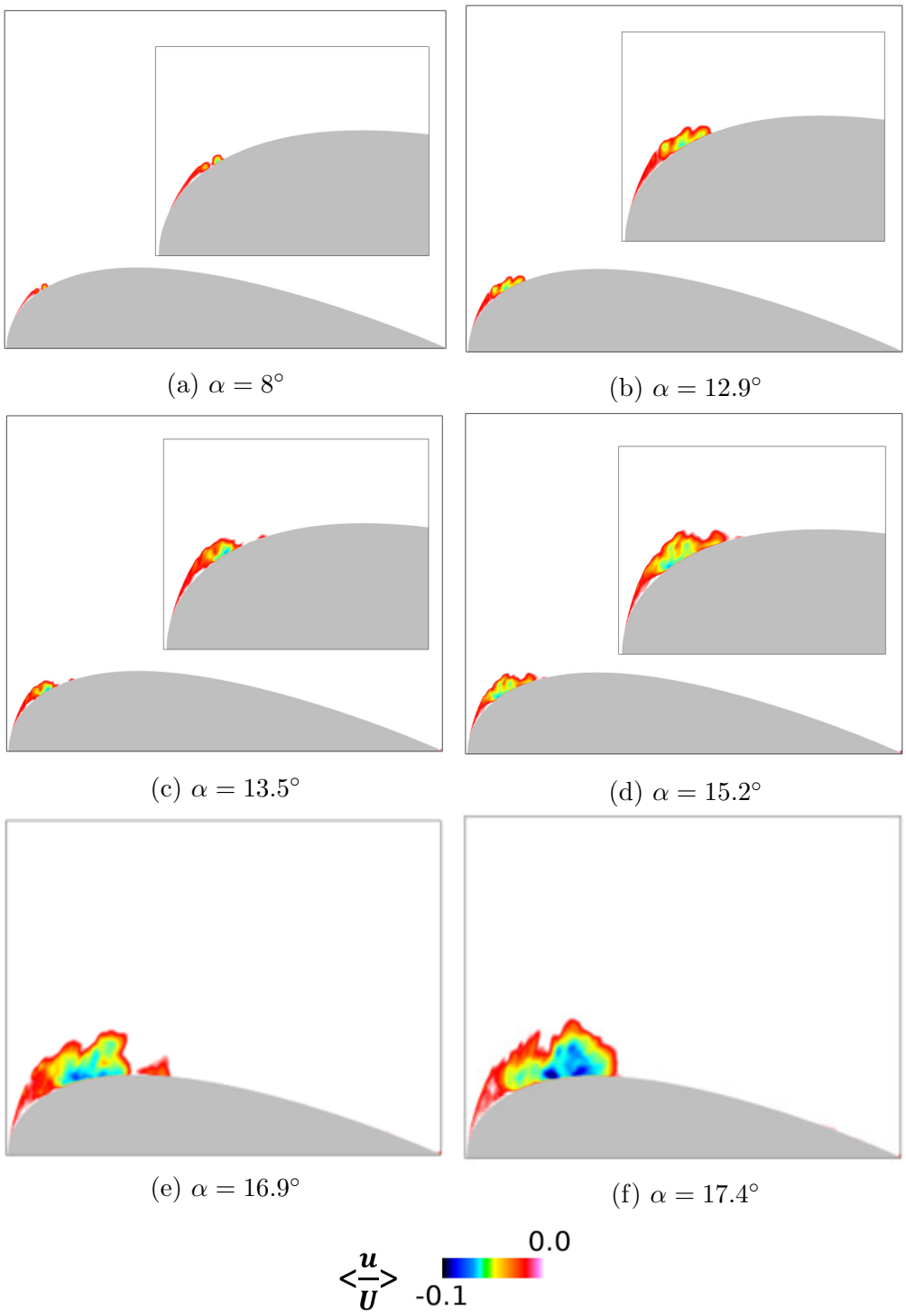

(a) $\alpha = 8°$

(b) $\alpha = 12.9°$

(c) $\alpha = 13.5°$

(d) $\alpha = 15.2°$

(e) $\alpha = 16.9°$

(f) $\alpha = 17.4°$

Figure 21: Spanwise-averaged streamwise velocity.

The closer looks at the vorticity magnitude profiles at the leading-edge in Fig. 22 also shed light on some of the discussed features regarding the leading-edge flow physics during the dynamic stall process. The separation bubble is indicted by the pockets of positive vorticity production. In Fig. 22(b), the shedding of vortices can be seen from the separated shear layer, which was also captured by Pruski and Bowersox [10]. The collapse of the LSB at the leading-edge can be seen at $\alpha = 16.9°$, where there is a rapid decrease in vorticity in the vicinity of the bubble in the previous stage. Another interesting point to note is the upwards propagation of the shear layer with increasing angle of incidence. This upwards propagation is caused by the clockwise rotation of the DSV which pushes the detached shear layer further from the airfoil surface.

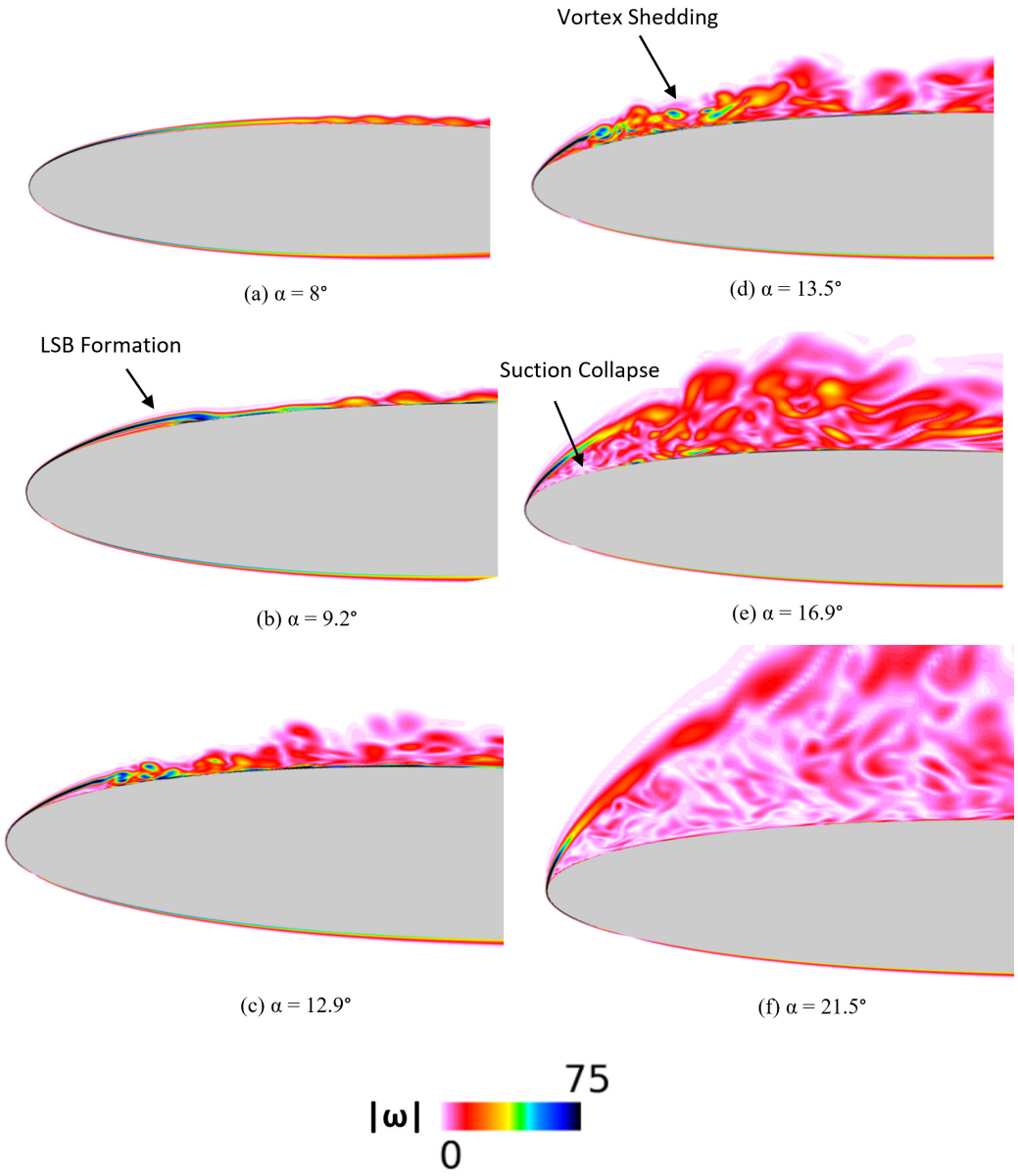

Figure 22: Near surface representations of instantaneous (mid-plane) vorticity magnitude.

From Fig. 23, a clearer representation of the separated shear layer behavior can be seen through the spanwise vorticity. As the angle of incidence is increased, there is a localized region of high spanwise vorticity at the leading edge of the airfoil, indicating the presence of a LSB. With larger angle of attack, the region of high vorticity continues to expand, indicated by Fig. 23(c). An interesting observation is that at $\alpha = 15.2°$ there exists the two distinct

reattachment branches in the flow, that were discussed previously. These reattachment zones present themselves as individual branches of vorticity that move towards the surface with a small pocket of low vorticity in between, which provide evidence on the kinks seen in pressure recovery region in the skin friction coefficient from Fig. 11(b). The complex nonlinear interactions in the leading-edge region just after suction is lost are what lead to the eventual formation of the DSV [37] which can be seen from Figs. 23(d)-(e). The strong interactions between counter-rotating vortices and the DSV can be seen at leading edge from the instantaneous spanwise vorticity in Fig. 23(f). There are distinct pockets of negative vorticity interacting with positivity vorticity prior to the DSV formation. Based on the spanwise averaged profiles, the instantaneous profile indicates that the negative vorticity contribution is arising from the separated flow downstream after suction collapse. Although researchers posed the question of if the LSB plays a significant role in the DSV process, after its initial separation, it does seem to have a significant effect on the dynamics of the DSV as a majority of the turbulent interactions seem to be stemming from the separated shear layer and its interaction with the reversed flow region just downstream after suction collapse. As mentioned previously, the bursting of the LSB is what initially triggers the process. It was found that a higher Reynolds number (10^6) by Benton and Visbal [12] that through high frequency actuation that the LSB bursting was suppressed, and the onset of stall was delayed. In this case, a gradual upstream propagation of trailing edge separation was observed rather than abrupt leading-edge stall. A further investigation would be required to assess the onset and formation of the DSV at this low Reynolds number if the bubble is not present or its bursting is suppressed by a means of flow control.

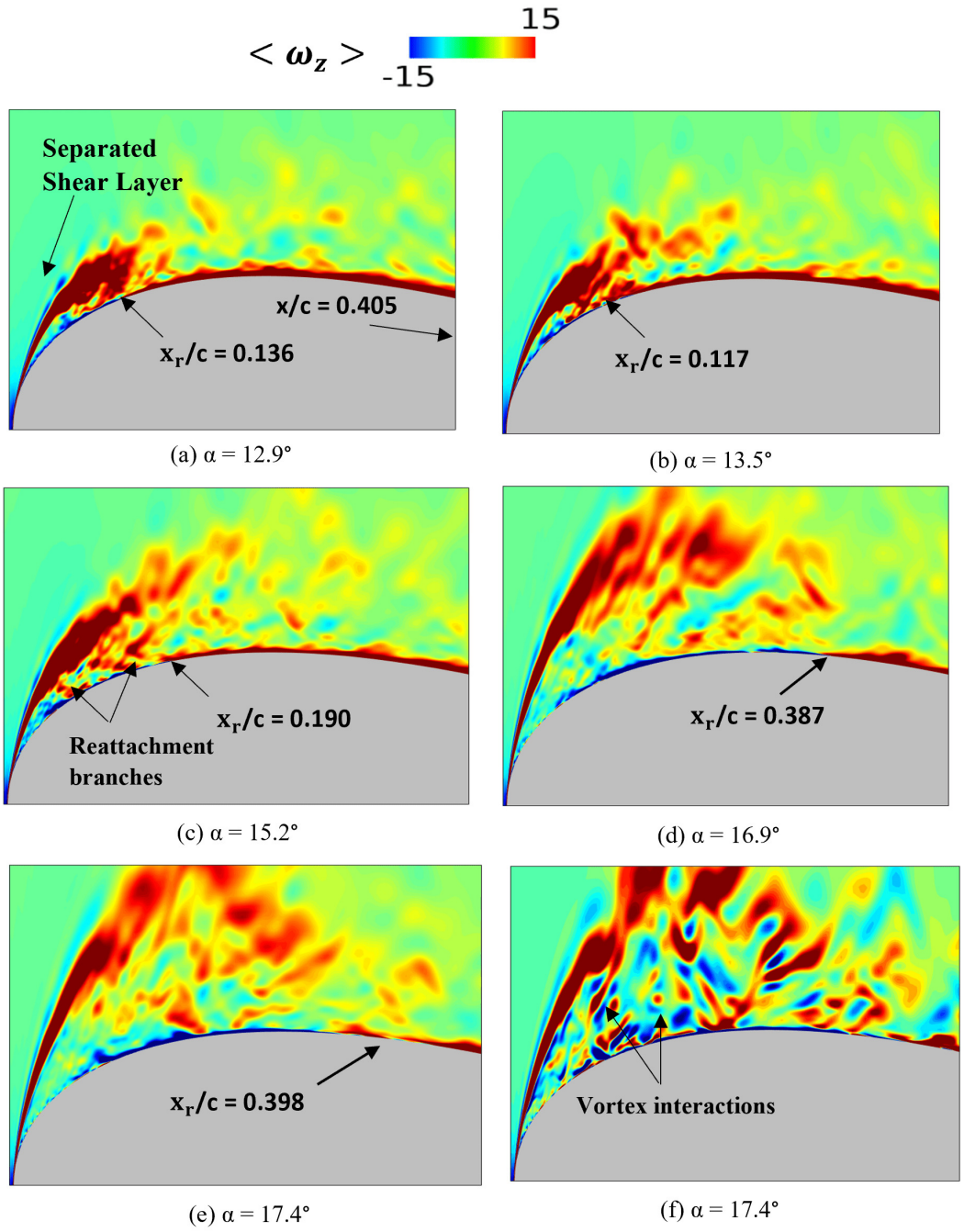

Figure 23: Spanwise-averaged contours of spanwise vorticity during DSV formation.

The time history of the dynamic stall process at $x/c = 0.05$ is depicted in Fig. 24 Prior to the collapse of the LSB there exists significant oscillations in the spanwise averaged pressure coefficient, seen in Fig. 24. These strong oscillations prior to the realization of the DSV were also noted in experimentation done by Lorber and Carta [43] on a NACA 0012 airfoil,

where they identified similar high frequency oscillations at the leading edge. Moreover, the difference in instantaneous and low pass filtered pressure in Fig. 24shows a significant spike prior to LSB formation, which might be crucial when considering implementing flow control technologies.

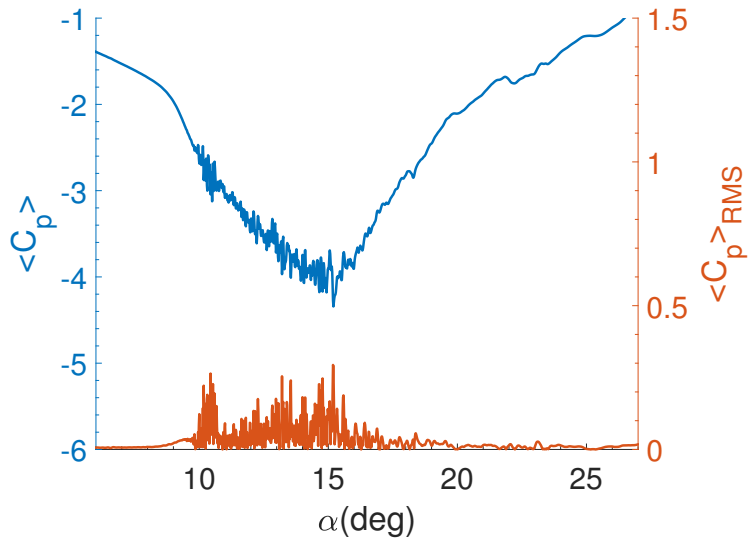

(a)

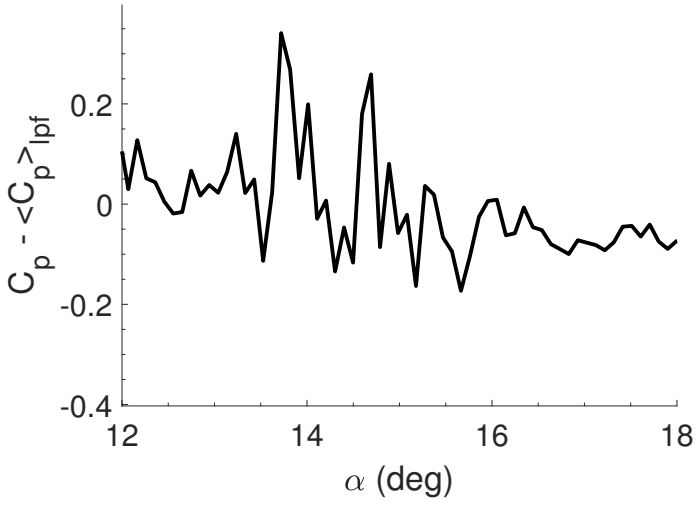

(b)

Figure 24: Instantaneous and root-mean-square surface pressure and b) instantaneous - low-pass-filtered surface pressure at $x/c = 0.05$.

4.5 Streamwise Vortex Sheets

One aspect of this process is the formation of long and slender streamwise vortices, which are depicted through the iso-surfaces of Q-criterion, or measure of the swirling strength, in Fig. 25. These vortices begin to form at higher angles of attack, roughly 18°, close to the stall point. It can be seen across Figs. 25(a)-(j) that the vortices are shifting across the span quite rapidly. This large sense of unsteadiness leads to the idea that these have a larger influence on the onset of dynamic stall, namely the detachment of the DSV. Figure 26 gives a clearer visual of the vortex sheets through the vortex core lines. Figure 27 shows the presence of these vortices from a front view, where there is the strong vorticity magnitude associated with these vortex sheets. It is hypothesized that these vortices have a significant impact on the overall dynamic stall process as their presence seems to affect the separation of the DSV. Due to their rotation around the streamwise axis, it is believed they can trigger the detachment of the DSV from the surface resulting in an earlier onset of stall. As seen in Figs. 25(i)-(j), these vortices remain in the flow field even beyond the stall angle. The unsteady propagation of these sheets across the span can be seen from the transient shift of the maximum regions of vorticity magnitude. These were briefly mentioned by Visbal and Garmann [1] but not investigated in depth.

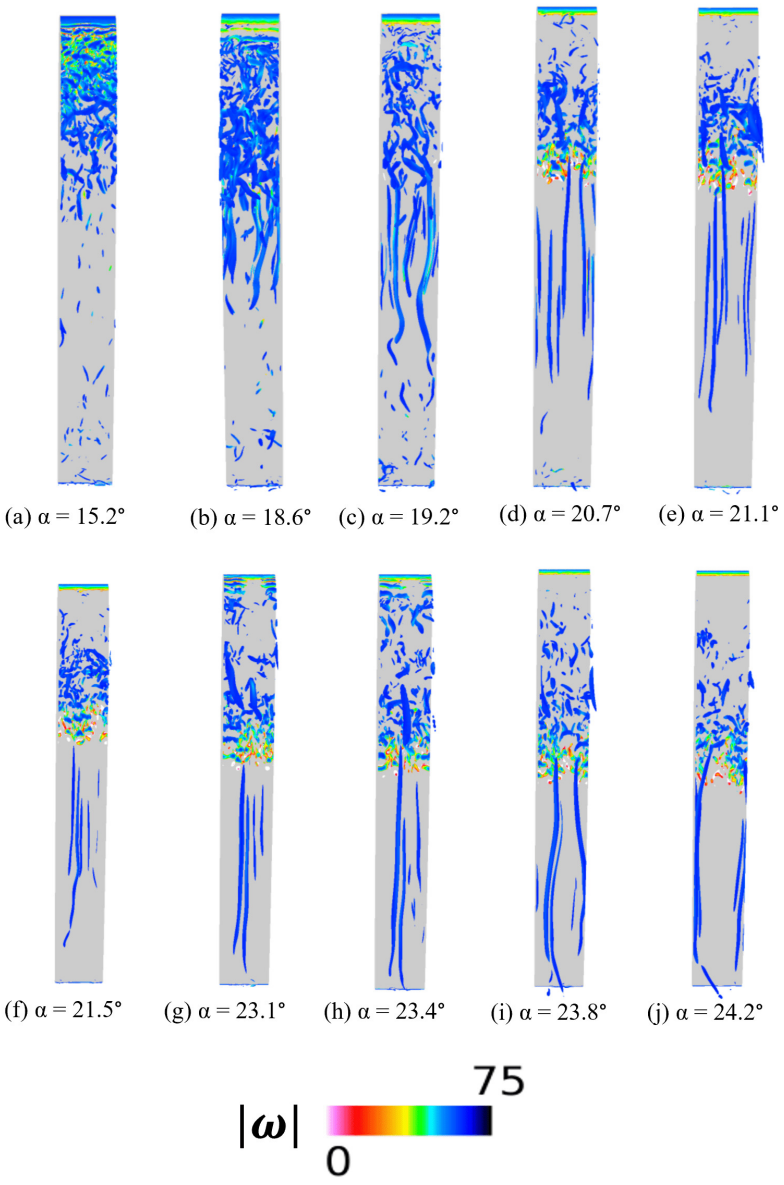

Figure 25: Iso-surfaces of Q-criterion = 100 colored by vorticity magnitude.

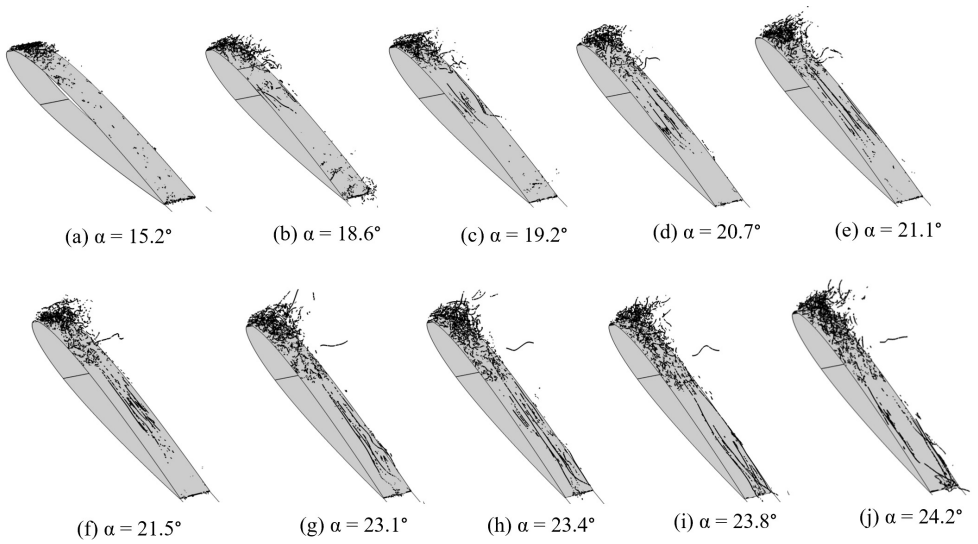

Figure 26: Vortex core lines across airfoil section.

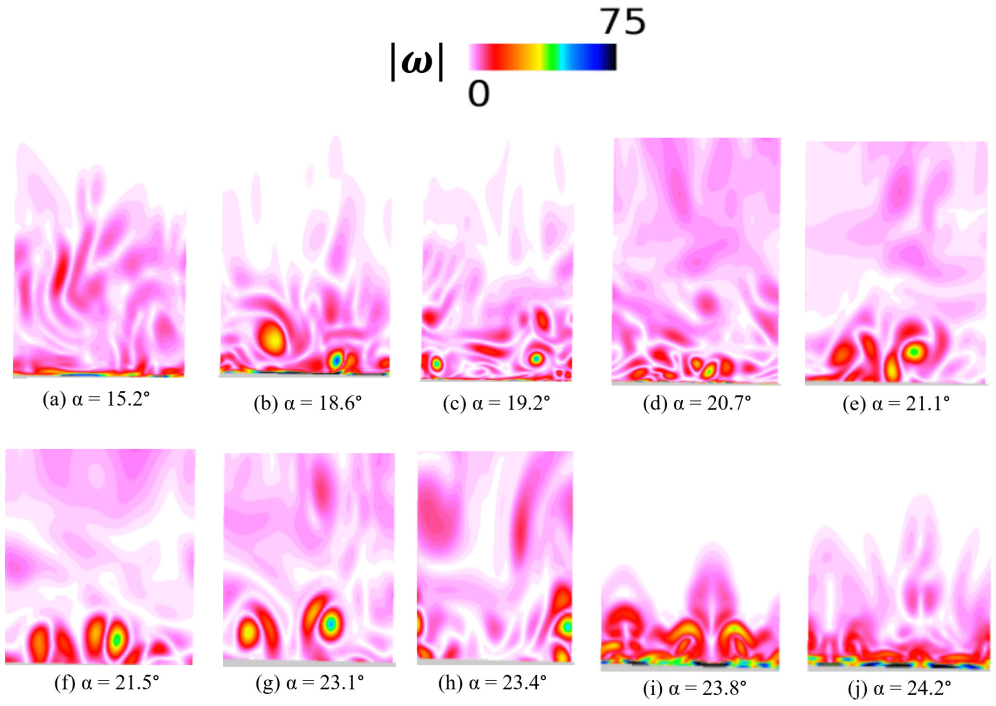

Figure 27: Front-view of vorticity magnitude at $x/c = 0.6$.

Chapter 5

Transition Model Study

5.1 Comparison of Transition Models

A more in-depth study is carried out on the 2nd grid configuration ($811 \times 200 \times 100$) to analyze the effect of turbulence models on the dynamic stall process, and compare them to benchmark LES results from Visbal and Garmann [1]. From Fig. 28, it can be seen that the predicted air loads remain relatively similar between all three turbulence models, despite the oscillations that are seen in the SA Medida-Baeder model at lower angles of attack. The SST Langtry-Menter Model shows the earliest onset of stall while both SA Models show similar points of stall onset. Differences can be seen when analyzing the flow physics in more detail, which is shown by the surface pressure and skin friction coefficients for all the transition models compared against LES [1] in Figs. 29 and 30.

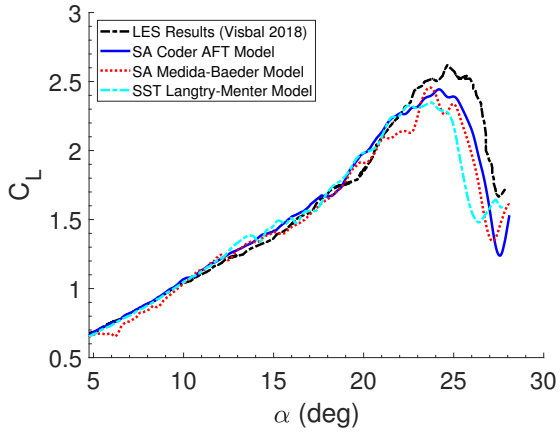

(a)

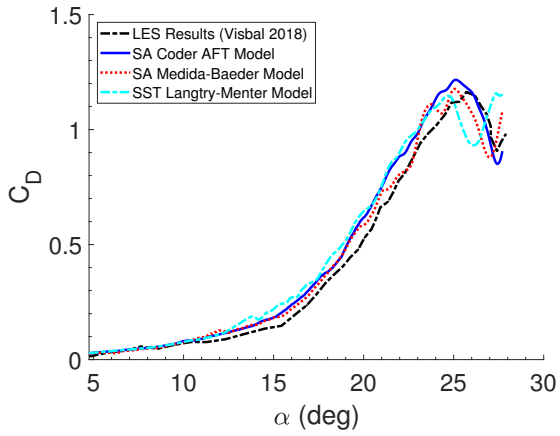

(b)

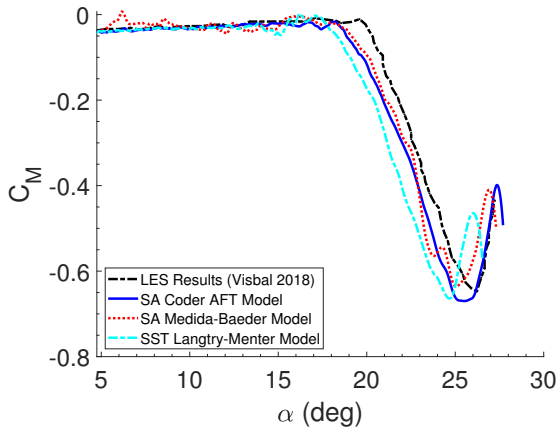

(c)

Figure 28: a) C_L, b) C_D, and c) C_M for the 3 different turbulence models studied.

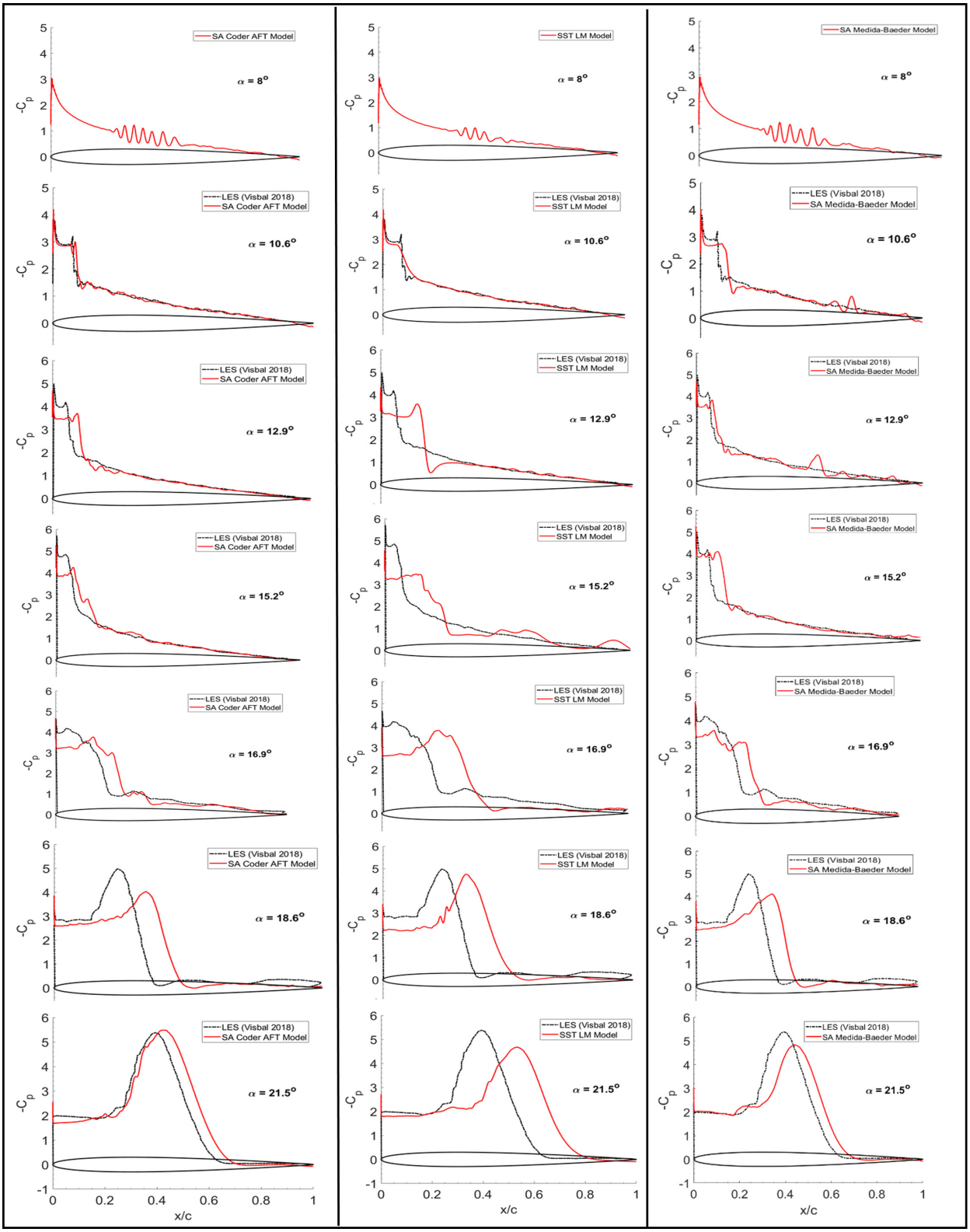

Figure 29: Spanwise-averaged C_p at the various stages of dynamic stall.

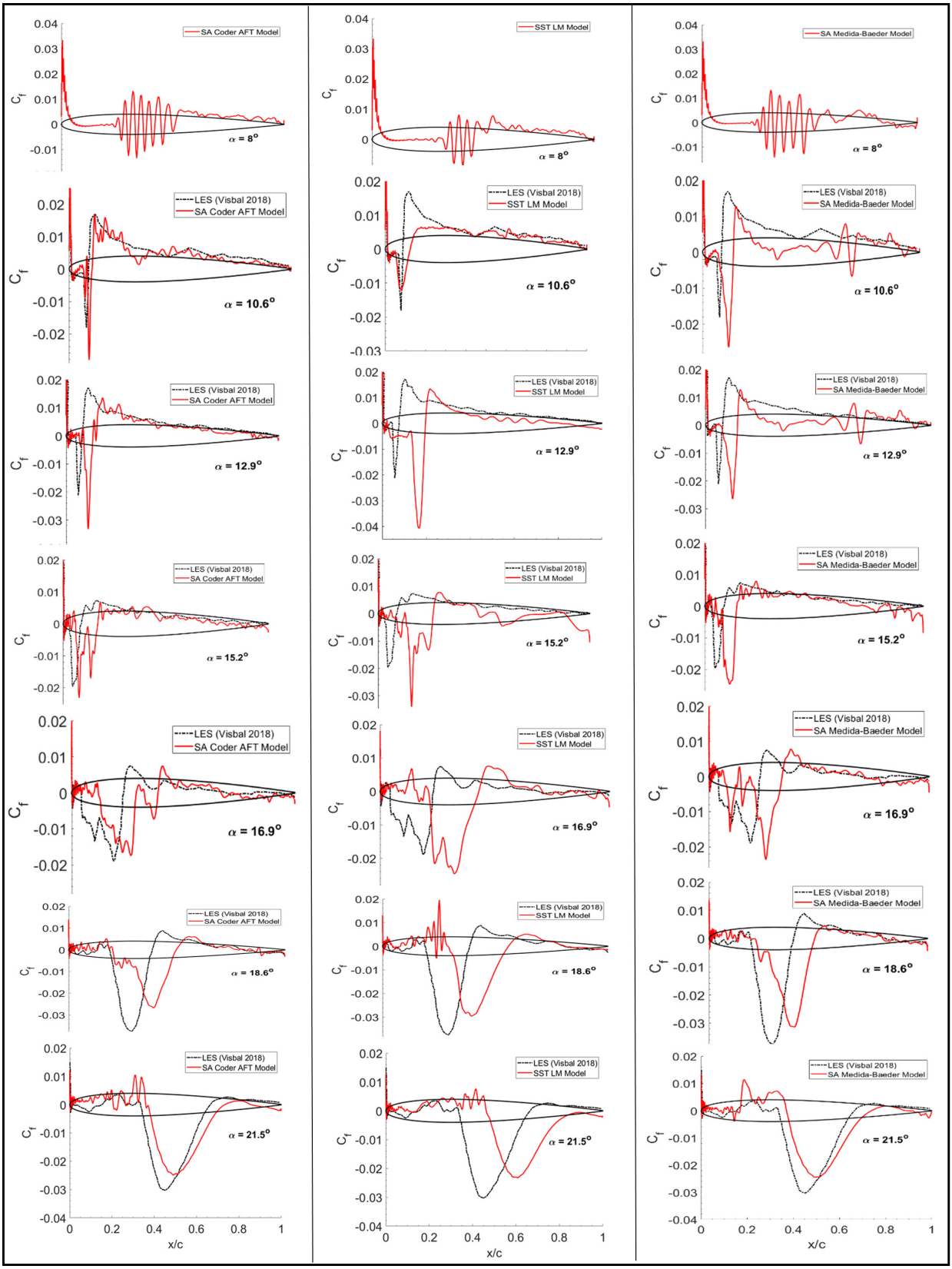

Figure 30: Spanwise-averaged C_f at the various stages of dynamic stall.

At (12.9°), it can be seen that for the SST Langtry-Menter (LM) Model, there exists a more expanded bubble, which can be seen through the wider pressure plateau and rapid pressure recovery, a feature that was not present with SA models investigated. The SA Medida-Baeder and SA Amplification Factor Transport (AFT) model show very close similarities at this stage in the dynamic stall process, however, the SA AFT model remains most accurate in terms of comparison with the LES results. The SST Langtry-Menter model shows the loss of suction much earlier than the previous two models, resulting in the earlier onset of dynamic stall. The dynamic stall process can still be considered relatively similar between all 3 cases, where during the pitch up motion, the transition point propagates upstream, and forms a LSB. For all cases, although not to the same extent, due to the unsteadiness, the LSB undergoes continuous expansion and contraction prior to collapse. This behavior was also present in benchmark static stall analysis by Pauley et al. [11] who identified similar unsteady expansion and contraction of the LSB. It can also be seen from Figs. 29 and 30 that there does not exist a significant amount of separated flow downstream prior to suction collapse which would have been indicated through a negative skin friction being present towards the trailing edge, further indicating that the type of stall investigated within the various turbulence models lies in parallel with leading edge stall through the pressure gradient induced burst of the LSB. The unsteady spikes in the spanwise averaged surface pressure at lower angles of attack ($\alpha = 12.9°$) - ($\alpha = 15.2°$) are associated with vortices being shed from the leading edge, just aft of the LSB, which can be seen in Fig. 31.

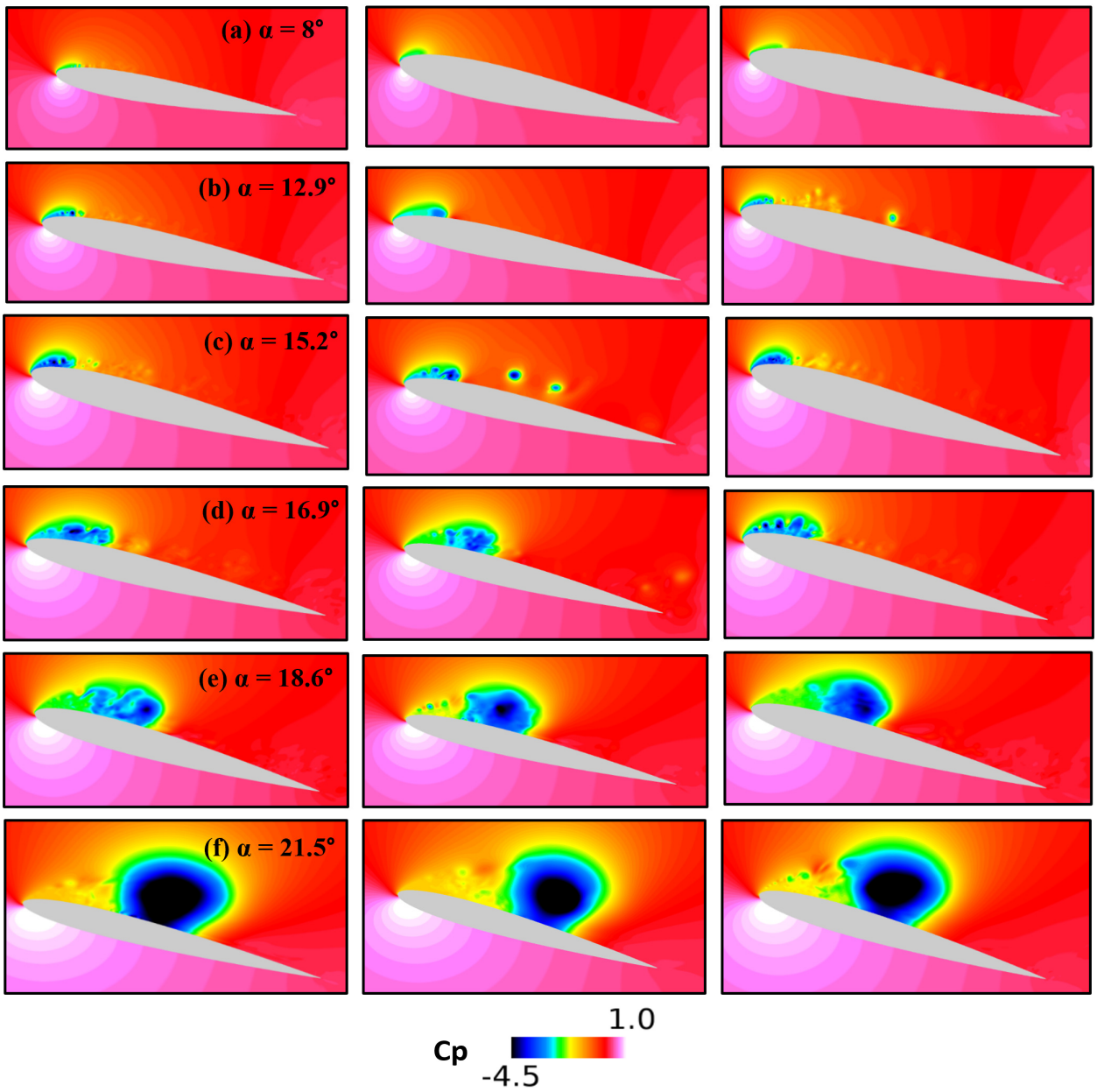

Figure 31: Spanwise-averaged C_f at the various stages of dynamic stall.

At $\alpha = 18.6^o$, for all transition models, the prediction of surface and skin friction show similar results. From Fig. 32, it can be seen that the duration of time from the DSV formation to its peak strength post suction collapse stretches across 3 stages, which is approximately over 2° angle of incidence. Hence, since the collapse of suction in the SST Langtry-Menter model is earlier on, this allows the DSV to reach its maximum strength during the while it was

still developing in the SA AFT and SA Medida-Baeder model. The interesting aspect to note here is that there exists a common ground for the flow physics post suction collapse, regardless of the transition model, as seen from the formation of the DSV itself. Although some of the flow features between both SA Models and the SST Model are different up to the point of the suction collapse, including the presence of an elongated bubble and indication of strong vortices being shed from the surface prior to LSB collapse, the events preceding the loss of suction are fairly similar, emphasizing the point that the LSB is the initial trigger for the dynamic stall process, more specifically, the formation of the DSV. The LSB's prior history before collapse seemingly doesn't have a significant impact on the overall process of DSV formation, as from Fig. 31, there exist differences in flow features leading up to LSB collapse, however, after $\alpha = 16.9^o$ up to the point of stall onset, the C_p profiles for all transition models show similarities with one another. The reason for stall being onset earlier with the SST model lies in the suction being lost early, allowing the DSV to form quicker and propagate off the surface before the SA Models.

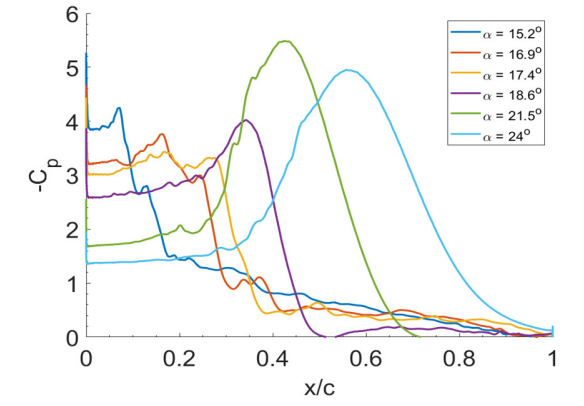

(a)

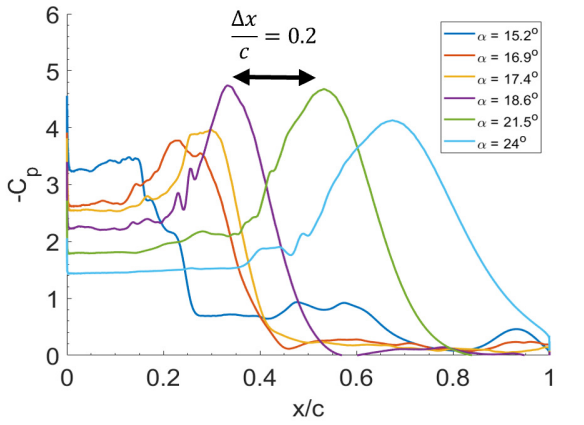

(b)

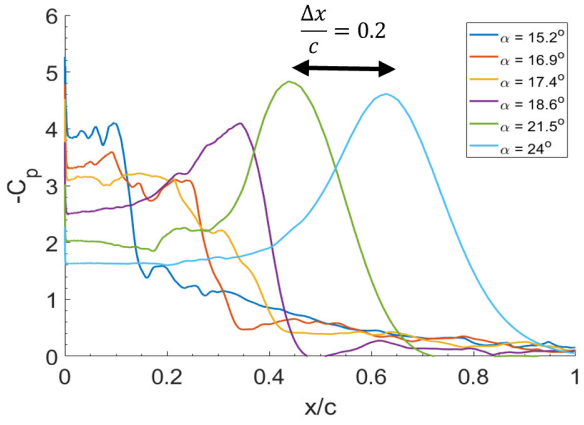

(c)

Figure 32: Spanwise-averaged C_p distributions depicting DSV formation/propagation for a) SA AFT, b) SST Langtry-Menter, and c) SA Medida-Baeder transition models.

5.2 Comparison with Large Eddy Simulations (LES)

Based on the predicted aerodynamic loads from Fig. 28, it is clear that DDES shows promising results in the predicted aerodynamic loads compared to LES [1], despite that the onset of lift stall was predicted slightly earlier using DDES with all turbulence transition models studied, and the peak lift coefficient was also underpredicted. When looking deeper at the overall flow physics and the leading-edge flow features, DDES seemed to capture the important phenomena that are presented in [1] including the formation and collapse of the LSB and the subsequent formation of the DSV. From the surface pressure and skin friction diagrams in Figs. 29 and 30, the biggest differences between the LES predictions are observed. In the earlier stages, for all 3 models there exist significantly more oscillations around the region of the LSB, even after spanwise averaging of the variables. Furthermore, LES computations [1] showed suction collapse at a later stage than the DDES results. While the mechanisms from which the DSV is formed line up with [1], the formation and propagation of the DSV occur at different rates, where the DDES shows slower formation and quicker propagation. Despite the differences presented, However, the performance of DDES was considered promising and within acceptable margins considering the temporal and spatial resolutions used in this investigation compared to that of LES [1]. Furthermore, another aspect to consider with DDES is that the use of RANS in the boundary layer will not give the true boundary layer behavior throughout the dynamic stall process, as small-scale turbulent features are averaged out. This can have a significant effect on the leading-edge flow physics observed.

Chapter 6

Conclusion

This thesis investigated the feasibility of DDES in terms of capturing important flow physics and predicting the aerodynamic loads during the dynamic stall process. Using James Coder's Amplification Factor Transport (AFT) Model, and a grid configuration comprising of roughly 16 million points, an in-depth study of the complex features during dynamic stall was carried out using NASA's OVERFLOW code. The key findings presented lie in parallel with studies done by a collection of researchers including Visbal and Garmann [1], McCroskey et al. [1], Pauley et al. [11], Gupta and Ansell [36], Mulleners and Raffel [37], and many others. The overall dynamic stall process comprised of the formation and collapse of a leading-edge laminar separation bubble (LSB), and the roll up of an unstable shear layer into a dynamic stall vortex (DSV) that propagates downstream. Upon investigation of these features, it was found that the LSB had a direct impact on the stall onset itself, as it served as the trigger for the particular events described leading up to the point of stall. Its importance is emphasized through analyzing the interactions between the separated flow upon loss of suction, and the separated shear layer emanating from the leading-edge whose complex nonlinear interactions lead to the formation of the DSV. It remains to be investigated how using flow control at this low Reynolds number would affect the process. Although flow control studies at higher

Reynolds number ($Re_c > 10^6$) suggest stall onset is delayed through bubble suppression and the method of stall onset is more from upstream propagation of trailing-edge separation. The regime of ($10^4 < Re_c < 10^5$) has not been analyzed in detail. All transition models within OVERFLOW showed significant promise in terms of the predicted aerodynamic loads as well as the complex flow physics in comparison with high resolution Large Eddy Simulations (LES) conducted by Visbal and Garmann [1]. The primary takeaway from these findings is that the use of DDES coupled with state-of-the-art transition modeling seems to be proficient in capturing the fundamental viscous mechanisms from which dynamic stall is onset. The overall behavior of the flow and the complex flow features at the leading-edge were able to be captured through not only the predicted pressure and skin friction profiles but also through the contours of pressure, vorticity, reversed flow, and turbulent kinetic energy. The effect of numerical methods with respect to the various transition models within OVERFLOW remains to be investigated in the framework of studying dynamic stall. It is unknown whether different numerical methods have a positive or negative effect on the predictions. Furthermore, it is evident that without the presence of experimental data, the question of prediction remains open ended. However, with the purpose of this study focusing on the capabilities of DDES, the validation of the process against experimental data was not of utmost importance, although sufficient experimental validation should be employed in future work for more accurate studies. It is also important to emphasize again that the dynamic stall process is heavily influenced by a variety of factors including compressibility, airfoil geometry, as well as the pitching rate. As McCroskey et al. [6] described, these factors influence the type of stall that is onset, as the process can be completely different from the sequence of events described in this report. Moreover, the predictions of the surface pressure at the leading edge showed significant oscillations prior to suction collapse, which could allow the possibility of flow control technologies being employed delay or mitigate the effects of dynamic stall. These distinct oscillations were in parallel with the findings of Visbal and Garmann [1], Lorber and Carta [43], and Pauley et al. [11]. The numerical

study carried out in this report has shown significant implications for future design work of the next generation of rotorcraft, as simulations on the temporal and spatial order of this study provide quick turnaround times, permitting more large-scale testing covering an array of flow conditions and design configurations. This research topic remains an open area of study given its significant complexity, however the promising results presented in this study can assist in further investigations at a reasonable computational cost.

References

[1] Visbal, M. R. and Garmann, D. J., "Analysis of Dynamic Stall on a Pitching Airfoil using High-Fidelity Large-Eddy Simulations," *AIAA Journal*, Vol. 56, (1), 2018, pp. 46–63.

[2] Smith, M. J., "An Assessment of the State-of-the-Art from the 2019 ARO Dynamic Stall Workshop," AIAA Aviation 2020 Forum, Virtual Event, June 15–19 2020.

[3] Leishman, J. G., *Principles of Helicopter Aerodynamics,*, Cambridge University Press, New York, second edition, 2006.

[4] Marques, P., "A Review of Active Blade Twist Technology: Part I – Actuation Concepts," *International Journal of Unmanned Systems Engineering*, Vol. 2, 2014, pp. 16–25.

[5] McCroskey, W., "The Phenomenon of Dynamic Stall," Nasa tm, Rhode-Saint-Genese, Belgium, March 1981.

[6] Carr, L., Mcalister, K., and Mccroskey, W., "Analysis of the Development of Dynamic Stall based on Oscillating Airfoil Experiments," Nasa tn, Pasadena, California, January 1977.

[7] Carr, L. W., "Progress in Analysis and Prediction of Dynamic Stall," *Journal of Aircraft*, Vol. 25, (1), 1988, pp. 6–17.

[8] Ham, N. D. and Garelick, M., "Dynamic Stall Considerations in Helicopter Rotors," *Journal of The American Helicopter Society*, Vol. 13, 1968, pp. 49–55.

[9] Shih, C., Lourenco, L., Van Dommelen, L., and Krothapalli, A., "Unsteady Flow Past an Airfoil Pitching at a Constant Rate," *AIAA Journal*, Vol. 30, (5), 1992, pp. 1153–1161.

[10] Pruski, B. J. and Bowersox, R. D. W., "Leading-Edge Flow Structure of a Dynamically Pitching NACA 0012 Airfoil," *AIAA Journal*, Vol. 51, (5), 2013, pp. 1042–1053.

[11] Pauley, L. L., Moin, P., and Reynolds, W. C., "The Structure of Two-Dimensional Separation," *Journal of Fluid Mechanics*, Vol. 220, 1990, pp. 397–411.

[12] Benton, S. I. and Visbal, M. R., "The Onset of Dynamic stall at a High, Transitional Reynolds Number," *Journal of Fluid Mechanics*, pp. 860–885.

[13] Langtry, R. B. and Menter, F. R., "Correlation-Based Transition Modeling for Unstructured Parallelized Computational Fluid Dynamics Codes," *AIAA Journal*, Vol. 47, (12), 2009, pp. 2894–2906.

[14] Schlichting, H., *Boundary Layer Theory*, McGraw-Hill, 7th edition, 1979.

[15] Liggett, N. and Smith, M., "Temporal Convergence Criteria for Time-Accurate Viscous Simulations of Separated Flows," *Computers and Fluids*, Vol. 66, 2012, pp. 140–156.

[16] Chan, W., "The OVERGRID Interface for Computational Simulations on Overset Grids," 32nd AIAA Fluid Dynamics Conference and Exhibit, St. Louis, Missouri, June 24–26 2002.

[17] Jespersen, D., Pulliam, T., Buning, P., Jespersen, D., Pulliam, T., and Buning, P., "Recent Enhancements to OVERFLOW," 35th Aerospace Sciences Meeting and Exhibit, Reno, Nevada, Januart 6–9 1997.

[18] Shum, J. G. and Lee, S., "Computational Fluid Dynamics Best Practices for 2D Dynamic Stall Predictions," AIAA Avitation 2020 Forum, Virtual Event, June 15–19 2020.

[19] Jain, R., Pape, A. L., Grubb, A., Costes, M., Richez, F., and Smith, M., "High-Resolution Computational Fluid Dynamics Predictions for the Static and Dynamic Stall of a Finite-Span OA209 Wing," *Journal of Fluids and Structures*, Vol. 78, 2018, pp. 126–145.

[20] Medida, S. and Baeder, J., "Numerical Investigation of 3-D Dynamic Stall using Delayed Detached Eddy Simulation," 50th AIAA Aerospace Sciences Meeting including the New Horizons Forum and Aerospace Exposition, Nashville, Tennessee, January 9–12 2012.

[21] Jia, Z. and Lee, S., "Aerodynamically Induced Noise of a Lift-Offset Coaxial Rotor with Pitch Attitude in High-Speed Forward Flight," *Journal of Sound and Vibration*, Vol. 491, 2021, pp. 115737.

[22] Jia, Z. and Lee, S., "Impulsive Loading Noise of a Lift-Offset Coaxial Rotor in High-Speed Forward Flight," *AIAA Journal*, Vol. 58, 2020, pp. 687–701.
doi: 10.2514/1.J058295

[23] Jia, Z., Lee, S., Sharma, K., and Brentner, K., "Aeroacoustic Analysis of a Lift-Offset Coaxial Rotor using High-Fidelity CFD/CSD Loose Coupling Simulation," *Journal of the American Helicopter Society*, Vol. 65, 2020.

[24] Menter, F., Kuntz, M., and Langtry, R., "Ten Years of Industrial Experience with the SST Turbulence Model," *Heat and Mass Transfer*, Vol. 4, 2003.

[25] Medida, S. and Baeder, J., "Application of the Correlation-based $\gamma - Re_{\theta_t}$ Transition Model to the Spalart-Allmaras Turbulence Model," 20th AIAA Computational Fluid Dynamics Conference, Honolulu, Hawaii, June 27–30 2011.

[26] Coder, J. G. and Maughmer, M. D., "Computational Fluid Dynamics Compatible Transition Modeling Using an Amplification Factor Transport Equation," *AIAA Journal*, Vol. 52, (11), 2014, pp. 2506–2512.

[27] Spalart, P. and Allmaras, S., "A One-Equation Turbulence Model for Aerodynamic Flows," 30th Aerospace Sciences Meeting and Exhibit, Reno, Nevada, January 6–9 1992.

[28] Liggett, N. D., *Numerical Investigation of Static and Dynamic Stall of Single and Flapped Airfoils*, Ph. d. thesis, Georgia Institute of Technology, 2012.

[29] Derlaga, J. M., Jackson, C. W., and Buning, P. G., "Recent Progress in OVERFLOW Convergence Improvements," AIAA Scitech 2020 Forum, Orlando, Florida, January 6–10 2020.

[30] Drela, M. and Giles, M. B., "Viscous-Inviscid Analysis of Transonic and Low Reynolds Number Airfoils," *AIAA Journal*, Vol. 25, (10), 1987, pp. 1347–1355.

[31] Coder, J. G., *Development of a CFD-Compatible Transition Model Based on Linear Stability Theory*, The Pennsylvania State University, 2014.

[32] Denison, M. and Pulliam, T. H., "Implementation and Assessment of the Amplification Factor Transport Laminar-Turbulent Transition Model," 2018 Fluid Dynamics Conference, Atlanta, Georgia, June 25–29 2018.

[33] Coder, J. G., Pulliam, T. H., and Jensen, J. C., "Contributions to HiLiftPW-3 Using Structured, Overset Grid Methods," 2018 AIAA Aerospace Sciences Meeting, Kissimmee, Florida, January 8–12 2018.

[34] Langel, C. M., Chow, R., Dam, C. C. P. V., Rumsey, M. A., Maniaci, D. C., Ehrmann, R. S., and White, E. B., "A Computational Approach to Simulating the Effects of Realistic Surface Roughness on Boundary Layer Transition," 52nd Aerospace Sciences Meeting, National Harbor, Maryland, January 13–17 2014.

[35] Hristov, G. and Ansell, P. J., "Poststall Hysteresis and Flowfield Unsteadiness on a NACA 0012 Airfoil," *AIAA Journal*, Vol. 56, (7), 2018, pp. 2528–2539.

[36] Gupta, R. and Ansell, P. J., "Unsteady Flow Physics of Airfoil Dynamic Stall," *AIAA journal*, Vol. 57, (1), 2019, pp. 165–175.

[37] Mulleners, K. and Raffel, M., "The Onset of Dynamic Stall Revisited," *Experiments in Fluids*, Vol. 52, 2011, pp. 779–793.

[38] McCroskey, W., Carr, L., and McAlister, K., "Dynamic Stall Experiments on Oscillating Airfoils," *AIAA Journal*, Vol. 14, (1), 1976, pp. 57–63.

[39] Kurelek, J. W., Lambert, A. R., and Yarusevych, S., "Coherent Structures in the Transition Process of a Laminar Separation Bubble," *AIAA Journal*, Vol. 54, (8), 2016, pp. 2295–2309.

[40] Chandrasekhara, M. S., Carr, L. W., and Wilder, M. C., "Interferometric Investigations of Compressible Dynamic Stall over a Transiently Pitching Airfoil," *AIAA Journal*, Vol. 32, (3), 1994, pp. 586–593.

[41] Lee, T. and Gerontakos, P., "Investigation of Flow over an Oscillating Airfoil," *Journal of Fluid Mechanics*, Vol. 512, 2004, pp. 313–341.

[42] Martin, J. M., Empey, R. W., Mccroskey, W. J., and Caradonna, F. X., "An Experimental Analysis of Dynamic Stall on an Oscillating Airfoil," *Journal of The American Helicopter Society*, Vol. 19, 1974, pp. 26–32.

[43] Lorber, P. F. and Carta, F. O., "Airfoil Dynamic stall at Constant Pitch Rate and High Reynolds Number," *Journal of Aircraft*, Vol. 25, (6), 1988, pp. 548–556.